International Journal of Plasticity 159 (2022) 103447

Contents lists available at ScienceDirect

International Journal of Plasticity

journal homepage: www.elsevier.com/locate/ijplas

Improved creep behaviour for a high strength Al-Li alloy in creep age forming: Experimental studies and constitutive modelling

Xi Wang, Qi Rong, Zhusheng Shi *, Jianguo Lin

Department of Mechanical Engineering, Imperial College London, London SW7 2AZ, UK

ARTICLE INFO

Keywords:
Creep age forming
Al-Li alloy
Threshold stress
Pre-stretching
Constitutive modelling

ABSTRACT

The creep deformation of 3rd generation 2xxx Al-Li alloys in creep age forming (CAF) is unsatisfactorily low due to its high strength and required low ageing temperature, especially for the commonly used T8 temper. Promoting creep deformation in such process will significantly reduce springback in CAF, making easier the springback compensation in tool design. In this study, two possible process routes of inducing increased creep deformation were explored, one by employing high applied stress to introduce small plastic strain in loading stage; and the other by conducting pre-deformation prior to creep-ageing. The creep behaviour with and without pre-deformation was investigated through creep-ageing tests under stresses ranging from 300 to 430 MPa at the ageing temperature of 143°C. Due to the decrease of threshold stress with introduced plastic strain in the loading stage and/or pre-stretching, a faster increase of creep strain with applied stress was observed for both methods when the applied stress surpassed 400 MPa. The strain promotion of the former was higher than the latter when above 415 MPa. A mechanism-based constitutive model was proposed, with additional work hardening equations to describe the relationship between threshold stress and dislocation density induced by plastic strain in the loading stage and pre-stretching, to model the microstructural evolution and reflect the nonlinear increase of creep strain with stress in both methods. The adequacy of this proposed unified model was demonstrated with good agreement with experimental data utilising both methods. The adaptability of the model in multiaxial case was verified using four-point bending CAF tests with the same Al-Li alloy.

1. Introduction

The fabrication of large panels has always been one of the focuses in aerospace industry, due to high demands in adopting these panels for outer skin such as wing and fuselage panels of aircrafts. Creep age forming (CAF) was particularly invented for integral fabrication of large scale skin panels (Holman, 1989). In traditional CAF process, creep deformation is utilised to deform the panel into target curvature at an elevated temperature. The panels are allowed to be deformed within the elastic region of the material, with low loading deflection and residual stress. However, the recent requirements of large and complex curvature for low cost and high fuel efficiency have significantly raised the difficulty in fabricating these panels (Rong et al., 2021). As a result, development of accurate constitutive relation of stress and creep strain in CAF further stands out as one of the primary challenges and keys to guarantee the successful and efficient fabrication through better springback compensation, in the way of reducing tooling and manufacturing costs.

* Corresponding author.
E-mail address: zhusheng.shi@imperial.ac.uk (Z. Shi).

https://doi.org/10.1016/j.ijplas.2022.103447
Received 10 June 2022; Received in revised form 13 September 2022;
Available online 25 September 2022

Creep is a time-dependent inelastic deformation behaviour under loading which has long been observed (Andrade, 1910; Krempl and Khan, 2003; Kassner, 2017), the rate of which is closely related to the microstructural evolution of the material in aspects of precipitation (Muñoz et al., 2009; Svoboda et al., 2016), dislocation (Oberson and Ankem, 2009; Shishvan, 2021), and grain size (Farrokh and Khan, 2009). Through adopting the intrinsic microstructures as internal state variables in the constitutive models, the creep deformation, damage, and failure behaviours have been adequately described with models based on two theories, the cavity growth mechanism (CGM) and the continuum damage mechanism (CDM) (Basirat et al., 2012; Yao et al., 2007). In the field of CAF, researchers have made great efforts in predicting the constitutive relation between the stress and the creep strain in creep-ageing over the past decades (Sallah et al., 1991; Ho et al., 2004a; Zhan et al., 2011; Li et al., 2017; Ma et al., 2018). The proposed constitutive relations have advanced from pure mathematical expressions such as power law and exponential law equations, to the unified mechanism-based models which focus on the creep behaviour within the primary and secondary creep stages and corresponding hardening mechanisms caused by evolutions of precipitates, dislocations, and solid solutes (Wang et al., 2021). In addition, further improvements have been achieved in capturing the recently observed creep-ageing behaviours through mechanism-based constitutive modelling: The double primary creep feature of AA2050 was adequately reflected by Li et al. (2017) through the dissolution of existing precipitates and the formation of new precipitates; The creep-induced stress relaxation in multi-step ageing of AA7050 was well predicted by Zheng et al. (2018); The improved creep behaviours achieved by applying large pre-deformation or initial loading to plastic region in stress relaxation, were respectively investigated and modelled recently (Liu et al., 2020; Rong et al., 2021; Yang et al., 2020)

On the other hand, the 3rd generation Al-Li alloys are characterised as advanced materials to substitute their predecessors with a more balanced synergy of strength, toughness, corrosion resistance and weight reduction (Brandon et al., 2012; Rioja and Liu, 2012). A further 7% weight reduction can be achieved by substituting AA2060 with its predecessors while maintaining the same performances (Brandon et al., 2012) and is desired for CAF application. T8 is the most widely used finish temper for these alloys, such as AA2060-T8 and AA2099-T8, however, their formability is limited with high strength in this temper (Brandon et al., 2012). It has been reported that low creep strain was generated in creep-ageing tests of 2xxx series aluminium alloys including Al-Li alloys (Zhou et al., 2021). Hence, new challenges have been raised in applying these advanced alloys in CAF, and methods to improve the creep formability of these high strength alloys are urgently needed.

With higher demands placed on more complex contour and larger curvature for CAF fabricated components, attentions have been drawn to the mechanism and modelling of large creep deformation induced by high stress/large initial strain in CAF in recent years. Yang et al. (2020) investigated the stress relaxation behaviour of AA2219 under high stresses up to 210 MPa which well surpassed its yield strength of 145 MPa. Stress relaxation behaviours in both elastic and plastic regions covering different initial strain levels ranging from 0.2% up to 2% were also investigated for AA6082 (Rong et al., 2021). Both studies manifested the happening of nonlinear change of relaxed stress when the applied stress and initial strain surpassed a certain value. This nonlinear change was attributed to the inducement of plastic deformation in the loading stage. In addition, by establishing a relation between plastic deformation-induced dislocations and varying threshold stress, the nonlinear change in stress relaxation have been modelled. However, apart from investigations of stress relaxation in the plastic region, little research has been conducted on constitutive modelling of large creep deformation in creep-ageing under constant stress. Furthermore, although the creep behaviour in plastic region was modelled by taking consideration of the effect of pre-existing dislocations on threshold stress, the initial plastic strain-induced dislocations in the loading stage were obtained through modified form of empirical equations (Rong et al., 2021; Yang et al., 2020). The understanding of the relationship among loading, initial dislocation density, and threshold stress in creep-ageing is still limited, and the linking with the practical loading process is not forthcoming.

In addition to increasing stress or initial strain in the loading stage, alternative treatment was also attempted to induce large creep deformation in CAF. An increased creep strain was achieved for 2xxx aluminium alloys undergoing solution heat treatment (SHT) and subsequent pre-deformation, when compared with the non-pre-deformed ones in creep-ageing (Liu et al., 2020; Xu et al., 2017; Yang et al., 2017). Further investigations found that creep deformation was decreased gradually with increasing pre-stretch levels for some SHTed Al-Li alloys (Hu et al., 2017; Zhang et al., 2019). Nevertheless, the effects of different applied stresses on pre-stretched material in creep-ageing have seldom been investigated. The pre-deformed creep behaviour in the primary stage was interpreted with Andrades's model (Liu et al., 2020), and the model has to be fitted with each applied stress, limiting its application in multiaxial CAF fabrication simulation in which a wide range of stresses can be involved.

For constant stress creep-ageing, the applied stress is limited to below the yield strength of the material to avoid entering the tertiary stage and consequent creep damage. With the limitation of the applied stress, little study has been carried out on methods to improve creep behaviour for high strength aluminium alloys, as well as the inducement mechanism and constitutive modelling of large creep strain for constant stress creep-ageing. This study aims to fill this research gap by exploring possible ways to increase creep deformation of high strength T8 temper 3rd generation Al-Li alloy in creep age forming. A broader scope of the material behaviour for the non-stretched and pre-stretched alloys in creep age forming is provided in this study, including the loading and creep-ageing stages with different applied stresses ranging from 300 to 430 MPa. The effects of different applied stresses on creep deformation were investigated through uniaxial creep-ageing tests under different stresses. The link between the pre-introduced dislocations with the subsequent creep behaviour of the material was studied in both materials. By considering the effect of pre-introduced dislocations on the material deformation in creep-ageing, a mechanism-based constitutive model with unified structure capable to reflect the creep deformation for both the non-stretched and pre-stretched materials was proposed and verified with experimental data. Additionally, the robustness of the proposed model is further investigated through its application to the multiaxial four-point bending CAF cases.

2. Experimental procedure

A 3rd generation 2xxx series Al-Li alloy was used in this study and the main chemical compositions are 0.6-0.9 wt.% Li, 3.4-4.5 wt.% Cu, 0.6-1.1 wt.% Mg and other minor compositions added in Al. The as-received material was in the form of 2, 4 and 6 mm thick sheets with T8 temper. The creep-ageing and tensile dog-bone specimens were cut along the rolling direction of the 2 mm sheets with a gauge length of 100 mm and width of 15 mm, detailed dimensions of which can be found in Wang et al. (2022).

Two groups of specimens were prepared for creep-ageing tests: one was the as-received and the other was the as-received plus 3% pre-stretching. For the convenience of following description, the creep-ageing tests and the derived strain for the as-received material are noted as CA (creep-ageing) and CAS (creep-ageing strain), while the pre-stretched ones are denoted as PCA (pre-stretched creep-ageing) and PCAS (pre-stretched creep-ageing strain). The experiment procedure for CA and PCA are schematically demonstrated in Fig. 1. Pre-stretching was carried out on a Sinotest DDL testing machine with a 50 mm gauge length extensometer at a strain rate of 0.001 s^{-1} at room temperature. The unloading point took into account the amount of strain of elastic recovery during unloading to obtain a 3% pre-deformation. The creep-ageing procedure was the same for both CA and PCA. The uniaxial creep-ageing tests were conducted on a Sinotest RDL50 tensile test machine with a Sinotest RH elevated temperature chamber, with the applied stresses ranging from 300 to 430 MPa at 143°C. The creep-ageing tests contained three stages including loading, creep-ageing, and unloading. When the specimen reached a stable temperature at 143°C, the load was exerted at a rate of 1 kN/min to the required value. After creep-ageing for the required hours, the specimen was unloaded, cooled down to room temperature with the furnace door opened. Additionally, interrupted creep-ageing and subsequent tensile tests were conducted to investigate the microstructural evolution and age hardening behaviour during CAF. Table 1 shows the stress levels and ageing times used in this study. For tensile tests, the same procedure as that for pre-stretching was employed and the yield stress was determined using 0.2% strain offset.

Transmission electron microscopy (TEM) studies were conducted to examine the microstructure and acquire quantitative data of precipitate size growth in the as-received material and the creep-aged ones under stresses of 300, 400, and 430 MPa at 6 and 15 h. TEM observation was accomplished on a TECNAI $G^2$20 machine with an acceleration voltage of 200 kV. For each sample, more than 120 precipitates were measured to acquire relatively reliable statistical information of precipitate diameter. X-ray diffraction (XRD) was adopted to measure the dislocation density of the as-received material and the creep-aged specimens at 6 and 15 h under 300, 400 and 430 MPa. The tests were conducted on Rigaku Smartlab with a 9 kW Cu Kα rotating anode (λ = 0.15406 nm) operating at 40 kV and 150 mA. The full width at half maximum (FWHM) of the obtained XRD line profiles was measured and used in the modified Williamson-Hall method to determine the dislocation density. Detailed descriptions regarding material's creep-ageing tests and microstructural investigation can be found in Wang et al. (2022).

Four-point bending CAF tests were carried out to demonstrate the validity of the model in the multiaxial case. Specimens with a dimension of 220 mm x 20 mm and thicknesses of 2, 4, 6 mm were adopted in the tests. Fig. 2 shows the setup and the dimensions. During tests, the upper cylinders were moved downwards with a loading displacement rate of 0.1 mm/s and were kept at the required position for creep-ageing at 143°C for 5 h. The loading displacement d_l was determined with Eq. (1) to reach a maximum surface stress σ_{max} of 430 MPa.

$$\begin{cases} d_l = \dfrac{2M}{Ebh^3}\left(3L_1L - 4{L_1}^2\right) \\ \sigma_{max} = \dfrac{6M}{bh^2} \end{cases} \tag{1}$$

where M is the generated moment, L_1 is the distance between the supporting and loading points and L is the half distance of the two supporting points as shown in Fig. 2. b and h are respectively the width and thickness of the specimen. E is the Young's modulus of the material at room temperature with the value of 69800 MPa. The calculated loading displacements for different thicknesses are shown in Table 2. The deflection of the four-point bending CAFed specimens were measured and used to compare with FE prediction.

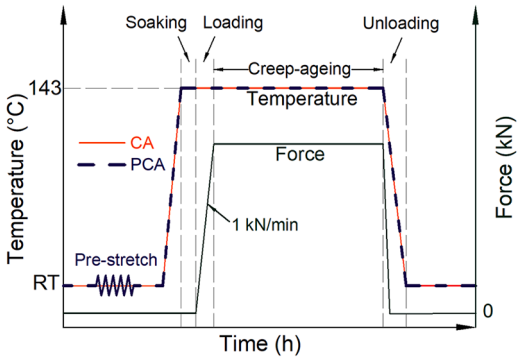

Fig. 1. Schematic of thermal and loading history for CA and PCA.

Table 1
Summary of creep-ageing test conditions.

Material condition	Stress (MPa)	Ageing time (h)
As-received T8 (CA)	300, 400, 430	3, 6, 15, 20
As-received T8 (CA)	360, 415, 422.5	20
Pre-stretched T8 (PCA)	300, 360, 400, 415, 422.5, 430	15

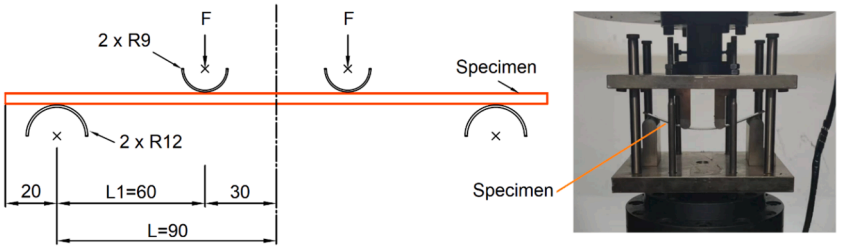

Fig. 2. Dimensions (mm) and setup of the four-point bending CAF tests.

Table 2
Loading displacements for different thicknesses to reach σ_{max}.

Thickness (mm)	Loading displacement d_l (mm)	Maximum surface stress σ_{max} (MPa)
2	18.7	430
4	9.2	430
6	5.9	430

3. Experimental results and analysis

3.1. Effect of applied stress on non-stretched creep deformation

Fig. 3 demonstrates the stress and strain evolutions during tensile and creep-ageing tests at the temperature of 143°C. Fig. 3a shows the stress-strain curves of the non-stretched and the 3% pre-stretched at 143°C at a strain rate of 0.001 s^{-1}. The 0.2% offset yield stress was 456 and 471 MPa respectively for the non-stretched and the pre-stretched. Based on the obtained stress-strain curves, a stress range of 300 to 430 MPa was selected to study the creep ageing behaviours of the alloy for both conditions. Fig. 3b demonstrates the stress and total strain evolutions in the first 0.5 h including the loading and initial creep-ageing stages under 430 MPa. The creep-ageing stage is deemed to begin at the time when the applied stress reaches its designed value which are kept constant afterwards. The strain at this point is denoted as initial strain and the strain accumulated in the creep-ageing stage is denoted as creep strain. It is noticed that the total strain does not increase linearly with stress at the later stage of loading to 430 MPa (see the inset in Fig. 3b). This is because that 430 MPa is above the proportionality limit and approaching the 0.2% offset yield strength of 456 MPa. Fig. 3c shows the total strain evolutions under 300, 400, and 430 MPa and the levels of corresponding initial strains. The creep strain evolution with ageing time is presented in Fig. 3d. A sharply increased creep strain can be observed when the applied stress is above 415 MPa. After 20 h creep-ageing, the accumulated creep strain under 415 MPa is about 2 times that for 400 MPa; and the creep strain under 430 MPa is over 7 times the strain under 400 MPa. From the creep strain results in Fig. 3d, the forming difficulty does exist when the applied stress is below 400 MPa: only 0.06% creep strain was obtained with creep-ageing at 400 MPa for 20 h.

To further illustrate the nonlinear creep deformation with increasing applied stress, creep strain ε_{cr} in respect of applied stress at the 20 h creep-ageing is plotted in Fig. 4a. A bilinear increase trend can be observed to intersect around 400 MPa in the relationship of applied stress and ε_{cr} in semi-logarithm form. As demonstrated in Fig. 3c and d, the creep strain evolution differs significantly in the first 2 h of creep-ageing in the primary stage, which can be attributed as the major cause resulting in the difference in the accumulated creep strain with increasing applied stress. Fig. 4a illustrates the comparison of the creep strain accumulated under different stresses in the first 2 h and later 18 h. A similar bilinear increase trend can be recognised in the first 2 h and later 18 h, which also intersects at the applied stress of 400 MPa. It can be observed in Fig. 4a that the contribution of the creep strain in the first 2 h exceeds the later 18 h and becomes the major accumulated creep strain for the total 20 h when the applied stress surpasses 400 MPa. It can also be observed in Fig. 3c that with different applied stress, different initial strains are accumulated at the end of loading stage, indicating that the strain accumulated in the loading stage can exert effects on the creep deformation in the subsequent creep-ageing stage, to which more attention should be paid. Fig. 4b shows the stress-total strain curves during the loading and creep-ageing stages for 415 and 430 MPa. From the curves in Fig. 4b, when the applied stress surpasses the value around 400 MPa in the loading stage, the stress-strain evolution begins to slightly diverge from the linear relationship shown as the dotted red line in the inset. σ_{end} in Fig. 4b is the stress at the end of the linear elastic stress-strain relation. The breakdown of the linear stress-strain relationship indicates that plastic strain was generated

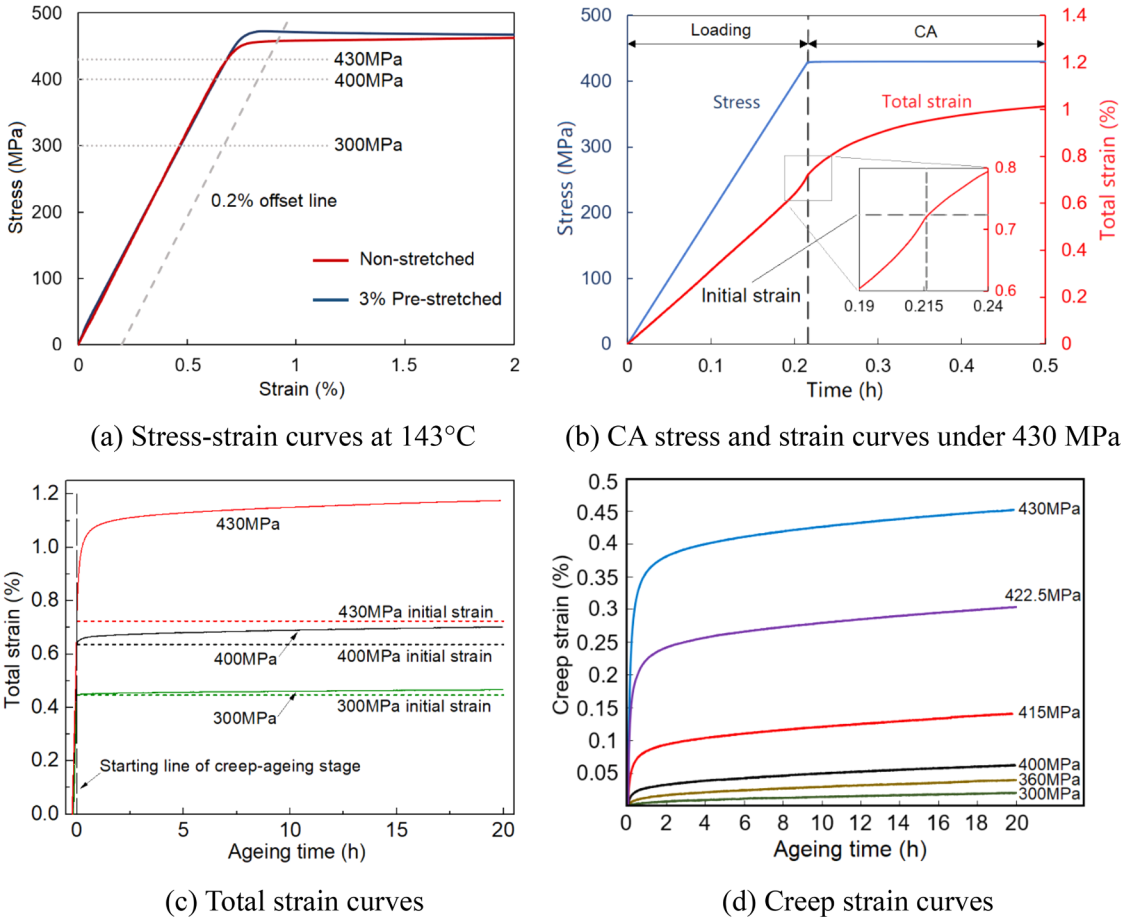

Fig. 3. Stress-strain curves for the as-received and pre-stretched materials at 143 °C and evolutions of strain and stress during creep-ageing tests of the as-received material under different stresses. (a) Stress-strain curves at 143°C; (b) CA stress and strain curves under 430 MPa; (c) Total strain curves; (d) Creep strain curves. The determination of the initial strain is demonstrated in (b).

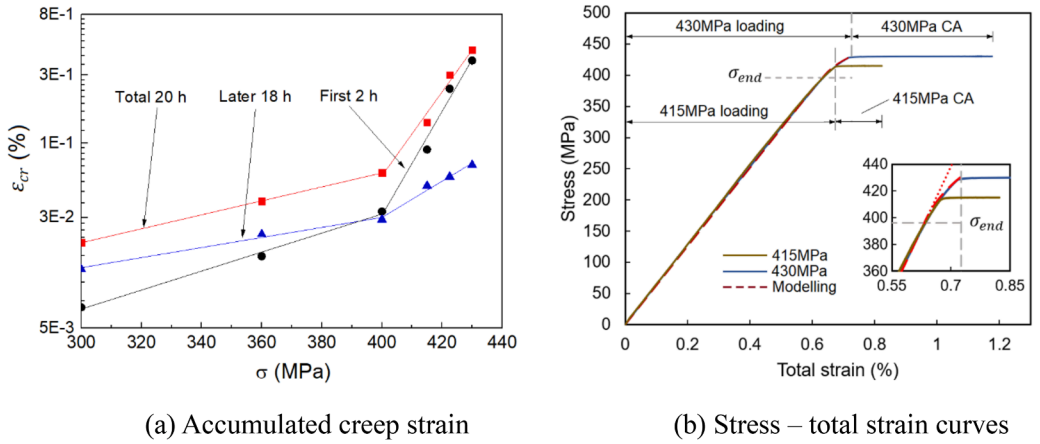

Fig. 4. The accumulated creep strain for the first 2 h, later 18 h and total 20 h under different stresses and the stress – total strain curves for the loading and creep-ageing stages under 415 and 430 MPa showing the deviation from linear stress-strain relation above σ_{end}. (a) Accumulated creep strain; (b) Stress – total strain curves. The dotted line in the inset in (b) is the extrapolation of linear stress-strain relation.

in the loading stage. A modelled stress-strain curve (red dashed line) for the loading stage to 430 MPa is also plotted in Fig. 4b, which will be discussed in Section 5.

3.2. *Effect of applied stress on pre-stretched creep deformation*

The creep-ageing behaviour for 3% pre-stretched material under the same selected stresses ranging from 300 to 430 MPa is presented in Fig. 5a, in which some results for the non-stretched as-received material are also plotted with the dashed lines for comparison. It clearly shows that the creep strain for the pre-stretched material is higher with stresses below 400 MPa, while the creep deformation of the as-received material surpasses the pre-stretched at applied stresses above 415 MPa. The variation of the ratio of PCAS to CAS as a function of the applied stress is shown in Fig. 5b. A general decreasing trend of the ratio can be observed, and the dropping rate increases when the applied stress surpasses 400 MPa. The PCAS to CAS ratio becomes lower than 1.0 when the applied stress is above 415 MPa, indicating that the effect of creep deformation enhancement by pre-stretching is decreasing with increasing applied stress for PCA. Fig. 5b also illustrates the variation of PCAS against the applied stress. Similar to Fig. 4a, a bilinear increase trend of ε_{cr} intersected at 400 MPa can be identified for PCA in Fig. 5b although the increasing rate is lower, indicating that similar mechanisms happen in both CA and PCA. Different to CAS, PCAS under 400 MPa in the first 2 h is higher than the later 13 h, demonstrating the promotion effect of pre-stretching on creep deformation. The stress-strain relationship in the loading stage of PCA is shown in Fig. 5c. As demonstrated in the figure, the breakdown of linear stress–strain relation happens around 400 MPa for PCA, similar to the loading curve of CA in Fig. 4b; while less obvious deviation from linear relationship of stress and strain can be identified for PCA when the load surpasses σ_{end}.

For creep deformation with 3% pre-stretched Al-Li alloys in T8 temper, in the stress ranging from 300 to 400 MPa, promotion of creep deformation was achieved when compared with the as-received material and the PCAS to CAS ratio is higher than 1.0, as shown in Fig. 5a and b. This promotion of creep deformation can be attributed to the reason that, with pre-stretching, an increased quantity of mobile dislocations are induced to decrease the creep resistance in the way of reducing threshold stress with increasing mobile

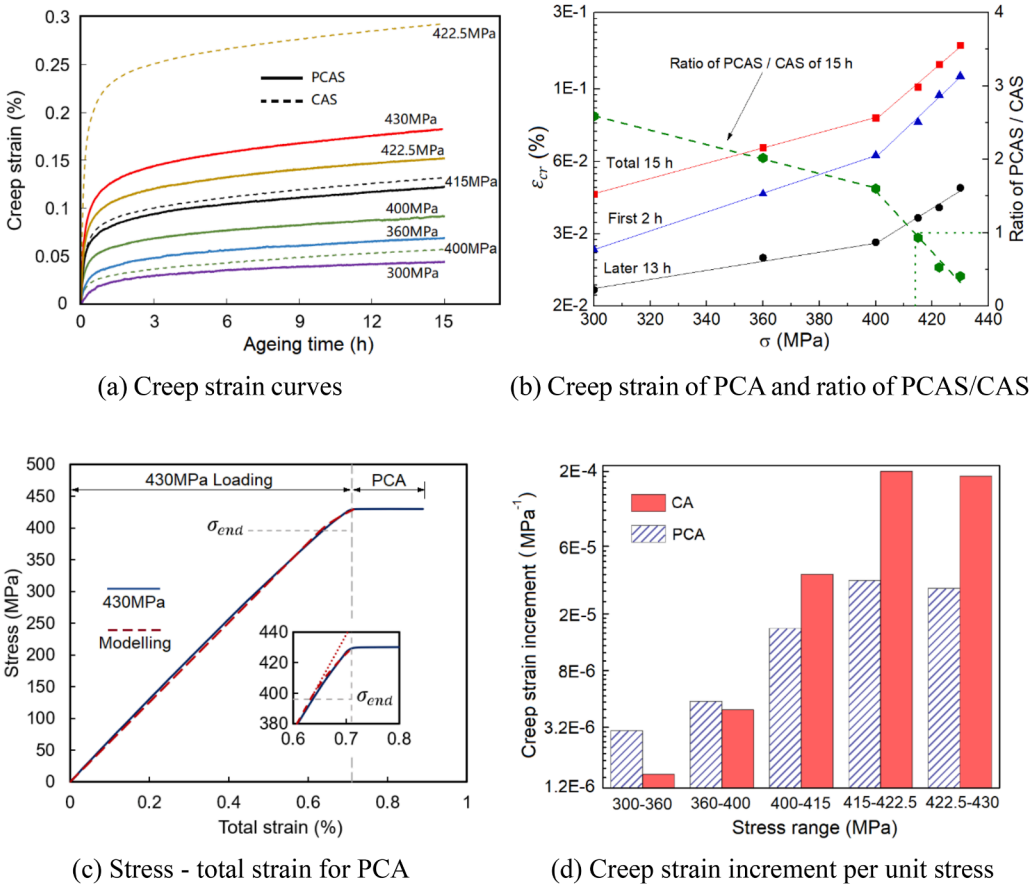

Fig. 5. Creep behaviour for the pre-stretched material, including creep strain curves under different stresses in comparison with CA cases, PCAS/CAS strain ratio, stress – total strain curves in the loading and creep-ageing stages, and the incremental rate per unit stress. (a) Creep strain curves; (b) Creep strain of PCA and ratio of PCAS/CAS; (c) Stress - total strain for PCA; (d) Creep strain increment per unit stress. The dotted line in the inset in (c) is the extension of linear stress-strain relation. In (d), the stress ranges used for calculating the increment rate are indicated.

dislocation slips (Yang et al., 2017). As a result, the creep deformation is largely enhanced especially in the primary creep-ageing stage.

On the other hand, a decreasing trend of the PCAS to CAS ratio with increasing applied stress was found. When the applied stress is below 415 MPa, the ratio of PCAS to CAS is higher than 1.0. It drops to below 1.0 when above 415 MPa. PCA shows a higher increase rate of creep strain per applied stress above 400 MPa than below 400 MPa, which is the same as the CA case, albeit with a much lower value. Fig. 5d demonstrates the results of the average creep strain increment per unit applied stress calculated from $(\varepsilon_{cr2} - \varepsilon_{cr1})/(x_2 - x_1)$, where ε_{cr1} and ε_{cr2} are respectively the creep strains accumulated at 2 h for the applied stresses x_1 and x_2. In the stress range from 300 to 360 MPa, the average strain increment per unit stress for PCA is about twice that for CA; while from 422.5 to 430 MPa, the increment for PCA drops to 0.16 times the value of CA. The trend of PCAS to CAS ratio with increasing applied stress, combined with

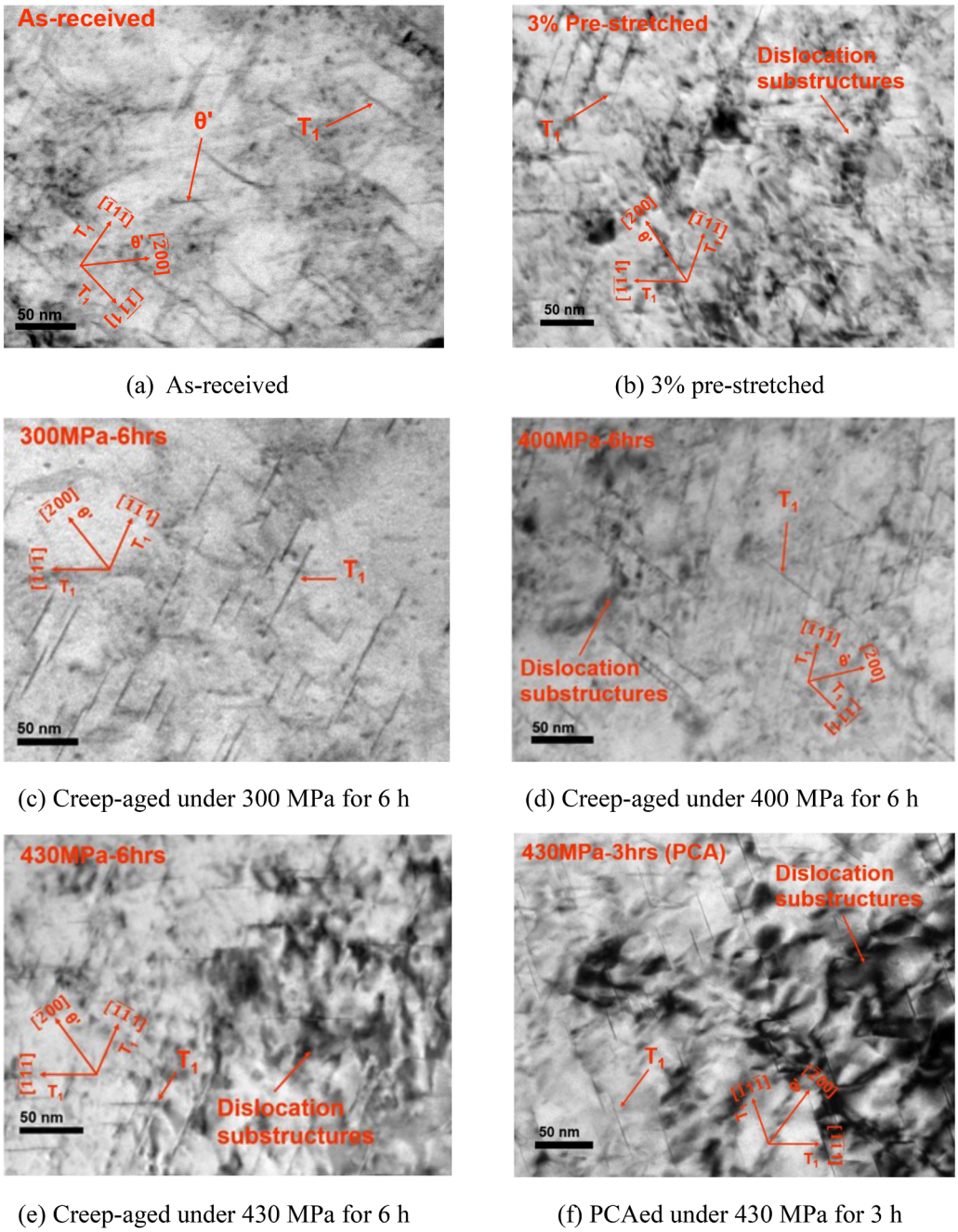

Fig. 6. TEM bright field images for the as-received, the pre-stretched, creep-aged and pre-stretched creep-aged (PCAed) specimens, showing precipitates and dislocation substructures. (a) As-received; (b) 3% pre-stretched; (c) Creep-aged under 300 MPa for 6 h; (d) Creep-aged under 400 MPa for 6 h; (e) Creep-aged under 430 MPa for 6 h; (f) PCAed under 430 MPa for 3 h.

the results of creep strain increment per unit stress in both conditions, shows a strong diminishing effect of creep deformation promotion for PCA when applied with higher stress. In addition, the creep strain increment stops increasing for both CA and PCA in the stress ranges of 415-422.5 MPa to 422.5-430 MPa.

The diminishing effect of creep deformation promotion with increased pre-stretching levels under the same applied stress had been reported in AA2050 Al-Li alloy with SHT (Zhang et al., 2019). It had been observed that when applied with the constant stress of 200 MPa, the creep deformation with pre-stretching level ranging from 2% to 6% was larger than the non-stretched but became lower when pre-stretching increased to 6% to 8% (Zhang et al., 2019). This observed decreasing trend of creep deformation with higher pre-stretching levels for Al-Li alloys can be mainly attributed to the increase of work hardening induced by more dislocations in the matrix through a higher extent of pre-deformation. It is known that work hardening is achieved by the hinderance to the mobile dislocations in ways of forming dislocation pileups and pinning with the precipitates (Dai et al., 2022; Lavrentev, 1980). Hence, with more dislocations being introduced in the alloy matrix, the pinning effect in the interactions between dislocations and precipitates is increased as stronger hinderance to the dislocation movement and therefore reducing creep deformation (Dai et al., 2022; Hu et al., 2017). It should also be noted that, more dislocations introduced in the matrix can induce more precipitates as stronger hindrance for dislocation movements, and therefore further reducing the creep deformation with increased pinning effect (Hu et al., 2017). However, the precipitation process of T_1 precipitate has already slowed down at T8 temper (Dorin et al., 2014), hence the effect caused by the finer precipitates is not considered to be a major contribution in the material used in this study. On the other hand, with a higher extent of pre-deformation, the work hardening is enhanced with an increasing quantity of dislocation pileups, which consequently reduces the duration of the primary stage of creep-ageing in which rapid growth of creep strain can be achieved (Lavrentev, 1980; Zhang et al., 2019). In the case of PCA in this study, when applied with higher stresses, larger dislocations were accumulated in the loading and subsequent creep-ageing stage, resulting in stronger work hardening for PCA and diminishing promotion of creep deformation. This will be further illustrated in the following section.

3.3. Microstructural evolution in creep-ageing

Fig. 6 presents the TEM images of the as-received, the pre-stretched, and the CA and PCA specimens. The images show clearly the two major precipitates in the material, i.e. T_1 and θ', and dislocation clusters after creep-ageing, consistent with precipitates observed in other Al-Li alloys (Chung et al., 2018). The dislocation density increases with increasing applied stress (c, d & e). In addition, as shown in the figure, due to the pre-stretching, more evident and denser dislocation substructures can be observed respectively in the pre-stretched (b) and PCAed (f) specimens when compared with the non-stretched (a and e). Previous study has shown that T_1 is the dominant precipitate, and the ratio of T_1 to θ' varies from 75:25 in the as-received state to 97:3 when creep-aged under 430 MPa for 15 h (Wang et al., 2022). Since T_1 is disc-shape precipitate, the diameter (or radius) of the precipitates is used to represent the precipitate size. The average diameters of T_1 precipitates as well as the dislocation densities at different conditions were measured and reported by Wang et al. (2022). Table 3 presents the results of precipitate size and dislocation density evolutions in creep-ageing of the as-received material obtained respectively by TEM observation and XRD tests. It shows that in general, the precipitates grow with ageing time and also with increasing applied stress, and the dislocation density has similar trend with ageing time and stress as the precipitates.

Different values of creep deformations were observed for CA and PCA when applied with the same stress ranging from 300 to 430 MPa in this study. Considering the above microstructural results, a schematic illustration for the relations between the observed different creep deformations and the corresponding microstructure states for the CA and PCA is proposed in Fig. 7. As shown in Fig. 5a and b, when applied with stresses lower than 400 MPa within a linear loading range with no additional dislocation being induced, a higher creep strain of PCA is obtained when compared with CA due to the greater quantity of mobile dislocations introduced through pre-stretching and lower threshold stress in the former, as illustrated in the left column of Fig. 7. The middle column in Fig. 7 shows that with the applied stress surpassing linear loading range, dislocations are introduced in the matrix for both CA and PCA, causing the reduction of threshold stress and non-linear increase of creep deformation as respectively observed in Figs. 4a and 5b for 415 MPa. On the other hand, due to the existence of pre-stretching-introduced dislocations for PCA, the continued introduction of dislocations by loading and subsequent creep-ageing can further increase the formation of dislocation pileups and enhance the pinning effect with the precipitates, which can lead to stronger work hardening and result in less creep deformation when compared with CA. When the applied stress is further increased to the highest level of 430 MPa, more dislocations are introduced in the matrix and the creep strain increment per unit stress stops rising: the results for 415 to 422.5 MPa and 422.5 to 430 MPa are almost the same, as shown in Fig. 5d. This steady increment indicates that work hardening is induced for both CA and PCA as illustrated in the right column of Fig. 7, while the work hardening of PCA is stronger than CA due to the pre-introduced dislocations by stretching, resulting in lower creep strain than CA as shown in Figs. 5a and 3d for 430 MPa. From the above analysis, it can be noted that when applied with the stress from 300 to 430 MPa, CA and PCA follow the same mechanism but are in different stages of hardening effect due to the pre-stretching-introduced

Table 3
Average values of precipitate diameter and dislocation density in creep-ageing of the as-received material.

Stress	Precipitate diameter (nm)			Dislocation density (10^{13} m^{-2})		
	0 h	6 h	15 h	0 h	6 h	15 h
300 MPa	35	40.2	52.5	1.7	2.4	2.7
400 MPa	35	52.8	52.3	1.7	4.5	4.9
430 MPa	35	48.5	50.8	1.7	5.6	6.3

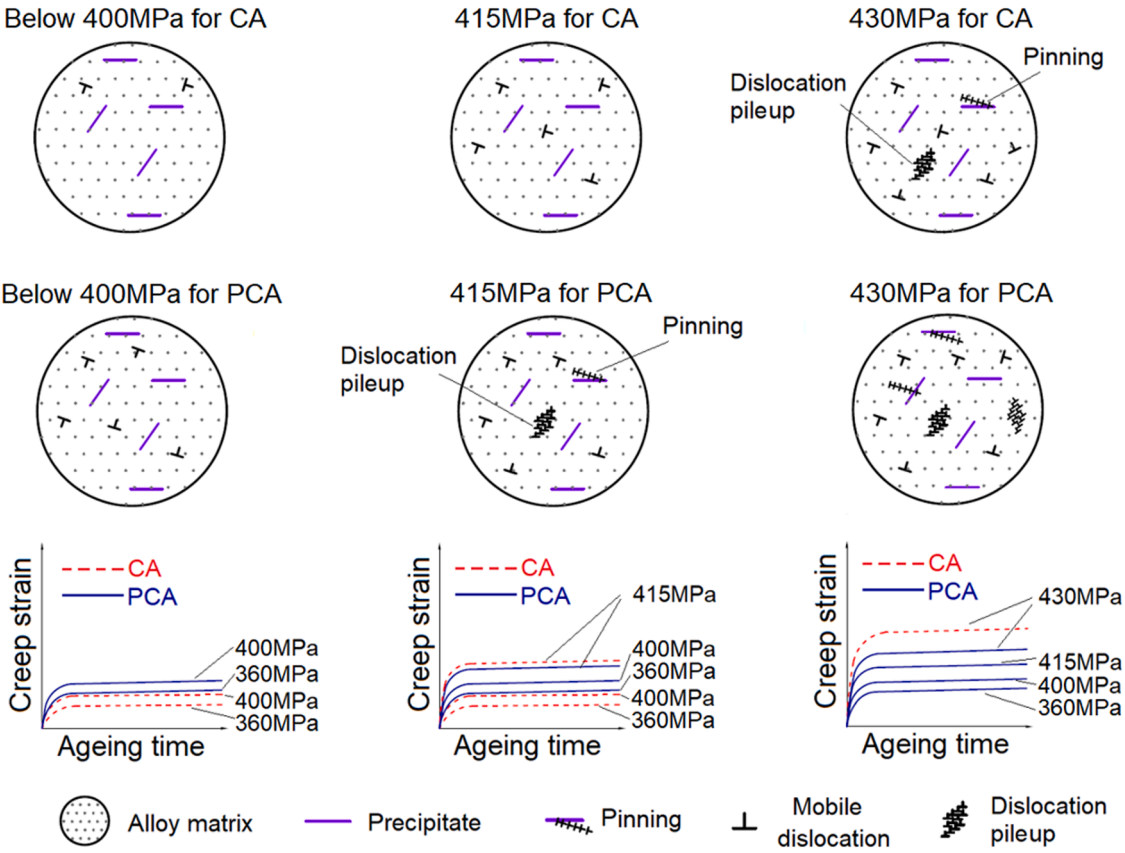

Fig. 7. Schematic illustration of the relations between the creep deformations and microstructure states for CA and PCA, showing the dislocation pileup and pinning by precipitate that led to diminishing promotion effect by PCA.

dislocation in PCA.

4. Constitutive model development

In the recent decade, the mechanism-based constitutive model has been widely adopted and is continuously being improved in studies of age hardening and deformation behaviour in creep-ageing (Li et al., 2017; Zheng et al., 2018; Li et al., 2019). A basic model structure composed of groups of constitutive equations to describe microstructural variables, hardening behaviours of material, and stress-creep strain relationship has long been established (Wang et al., 2021). In this study, by combining a work hardening model in the loading stage, a mechanism-based constitutive model is developed to describe the increased creep deformation behaviour observed in creep-ageing for the non-stretched and the pre-stretched materials with a unified structure. The proposed model consists of four groups of constitutive equations:

(1) Work hardening model proposed to obtain initial plastic strain and corresponding dislocation density at the end of the loading stage (beginning of creep-ageing stage) to determine the threshold stress for creep.
(2) Microstructural constitutive equations to describe precipitate growth and dislocation density evolution during creep-ageing.
(3) Strengthening equations to express material hardening induced by microstructural evolutions (precipitates and dislocations).
(4) Macro stress-creep strain relationship expressed with a sinh-law function which can reflect the effects of internal microstructural variables on macro creep deformation behaviour.

4.1. Threshold stress determination

4.1.1. Initial threshold stress

Threshold stress σ_{th} is the critical value under which creep cannot be induced (Rong et al., 2021; Yang et al., 2020). The presence of the threshold stress has long been identified in creep of different alloys (Dunand and Jansen, 1997; Krug and Dunand, 2011; Wang et al., 2017). It has been established that threshold stress is the resistance stress generated when overcoming second phase obstacles in

deformation-induced dislocation movements (dislocation climb/glide) (Wang et al., 2017). When threshold stress is considered, creep deformation behaviour is no longer considered to be only affected by the total stress σ, instead the stress $(\sigma - \sigma_{th})$ should be adopted. As a result, the steady state creep rate $\dot{\varepsilon}$ can be written as (Dunand and Jansen, 1997):

$$\dot{\varepsilon} = A(\sigma - \sigma_{th})^n \exp\left(\frac{-Q_a}{RT}\right) \tag{2}$$

where A is a temperature dependant material constant related to the shear modulus; n is the stress exponent as an index indicating the dominant creep mechanism; Q_a is the activation energy. R is the gas constant; T is the absolute temperature in Kelvin degree.

To determine initial threshold stress σ_{th0} with the fit value of n for the as-received and pre-stretched materials, a linear extrapolation method to estimate the initial threshold stress with constant temperature is employed by adopting the logarithm form of Eq. (2), i.e. $\ln(\dot{\varepsilon}) = n\ln(\sigma - \sigma_{th}) + \ln(A\exp(-Q_a/RT))$. The lower stress group including 300, 360 and 400 MPa under which linear elastic stress-strain relation is maintained in the loading stage was selected for the initial estimation. If σ_{th} was not considered in Eq. (2), n values of 2.9 and 1.8 were obtained respectively for CA and PCA with the average creep strain rate in the steady state ($\dot{\varepsilon}$ drops below 1.0×10^{-8} s^{-1}) of the selected stress range, indicating that the diffusion creep mechanism, i.e. with n ranges from 1 to 3 (Chokshi, 2008), was dominant for both material conditions when creep-aged within lower stress group.

The procedure of the method can be generalised as follows: (i) Given a trial value of σ_{th0} (the initial trial values of σ_{th0} were zero with n of 2.9 and 1.8 respectively for CA and PCA), a fitting line $\ln(\dot{\varepsilon}) = a_1\ln(\sigma - \sigma_{th0}) + b_1$ for CA and PCA conditions can be obtained. Fig. 8a demonstrates such fitting lines with trial σ_{th0} values of 105 MPa for CA and 85 MPa for PCA. According to the logarithm form of Eq. (2), n is equivalent to a_1. (ii) With the acquired value of n ($= a_1$), another fitting line for CA and PCA conditions as $\dot{\varepsilon} = a_2(\sigma - \sigma_{th0})^n + b_2$ can be obtained, as shown in Fig. 8b. The derived fitting equation becomes $\dot{\varepsilon} = b_2$ when $\sigma = \sigma_{th0}$. If the criterion $|b_2| \leq \dot{\varepsilon}_{300}/100$ is satisfied ($\dot{\varepsilon}_{300}$ is the steady state creep strain rate at 300 MPa), b_2 can be considered as a negligible creep strain rate $\dot{\varepsilon}$ achieved with $(\sigma - \sigma_{th0})$, and σ_{th0} can be deemed as the suitable initial threshold stress under which creep is not induced. If not, the above steps (i) and (ii) are repeated for different σ_{th0} values. It can be noticed that the initial threshold stress determined for CA is larger than PCA (105 vs 85 MPa), which is consistent with the observation that the creep deformation of PCA is larger than CA under 300, 360, and 400 MPa. To differentiate, σ'_{th0} will be used for the initial threshold stress for PCA case in the following sections.

4.1.2. *Effect of pre-existing dislocation*

The breakdown of the linear stress-strain relationship and the introduction of plastic strain in the loading stage, as noticed in Figs. 3 and 4, can induce the nonlinear increase of creep deformation at the primary creep-ageing stage with the applied stress levels. A similar phenomenon was found in stress relaxation; When the initial loading was in the plastic region, a nonlinear increase of relaxed stress was identified (Rong et al., 2021; Wang et al., 2017; Yang et al., 2020). The promotion of creep deformation and reduction of creep resistance with the plastic strain-introduced dislocations have been reported in many studies (Liu et al., 2020; Rong et al., 2021; Yang et al., 2020). There are mainly two reasons for this effect: First, with increasing mobile dislocations introduced in the matrix, the duration of the primary stage in creep-ageing is extended which can lead to an evident rise of the accumulated total creep strain; Second, when adopting high stress, plastic strain and corresponding dislocations can be induced in the alloy matrix. Dislocation glide then becomes the dominating mechanism, causing a significant reduction of creep resistance/threshold stress with an estimated 10 times lower dragging force in dislocation movement compared with dislocation climb (Mordehai et al., 2008). When considering the lowered creep resistance caused by the induced dislocation at higher stress, different forms of exponential decay functions were proposed to express the dramatic drop of threshold stress with increasing dislocation density (Wang et al., 2017; Yang et al., 2020). A term $n_1\overline{\rho}_0^{m_1}$ was introduced to account for the reduction of threshold stress due to the existence of plastic strain-induced initial

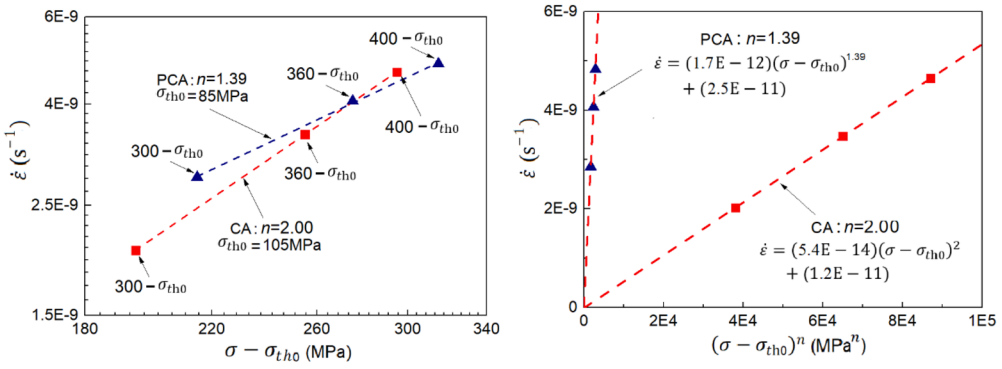

(a) Logarithmic plot of $\dot{\varepsilon}$ with $(\sigma - \sigma_{th0})$ (b) Plot of $\dot{\varepsilon}$ with $(\sigma - \sigma_{th0})^n$

Fig. 8. Determination of initial threshold stress with plots of $\dot{\varepsilon}$ against respectively $(\sigma - \sigma_{th0})$ and $(\sigma - \sigma_{th0})^n$ for CA and PCA. (a) Logarithmic plot of $\dot{\varepsilon}$ with $(\sigma - \sigma_{th0})$, shows the fitting lines with the initial threshold stress of 105 MPa for CA and 85 MPa for PCA; (b) Plot of $\dot{\varepsilon}$ with $(\sigma - \sigma_{th0})^n$, demonstrates that the second term in the well fitted creep strain rate equation is negligible.

dislocation density $\overline{\rho}_0$ (Yang et al., 2020). Thus, the threshold stress in creep-ageing can be expressed in the form of a ramp function equation (RFE) as:

$$\sigma_{th} = \left\langle \sigma_{th_0} - n_1 \overline{\rho}_0^{\,m_0} \right\rangle \tag{3}$$

where $\langle \mathbf{X} \rangle$ is Macaulay brackets, indicating a ramp function in which negative values return 0; σ_{th_0} is the intrinsic threshold stress of the as-received material under which creep cannot be induced; n_1 and m_0 are material constants. $\overline{\rho}_0$ is the normalised dislocation density generated in the loading stage and is defined as $\overline{\rho}_0 = (\rho_0 - \rho_i)/(\rho_m - \rho_i)$, ρ_i is the initial dislocation density at the as-received state, ρ_m is the dislocation density at the saturated state. Based on the definition, $\overline{\rho}_0$ value can range from 0 to 1.

When adopting Eq. (3) to describe the threshold stress σ_{th}, σ_{th} decreases at an increasing rate with the increase of $\overline{\rho}_0$, as demonstrated with the dotted curve in Fig. 9. Consequently, threshold stress has a sudden turn when it drops to zero without smooth transition, which can cause an abrupt change in predicted creep strain. Hence, to eliminate this issue, a modified equation is given in the form of reversed exponential equation (REE) as:

$$\sigma_{th} = \sigma_{th_0} / (1 + \exp(n_{1a} \overline{\rho}_0^{\,m_{1a}} - B)) \tag{4}$$

where n_{1a}, m_{1a}, B are material constants. Fig. 9 shows the schematic relation of σ_{th} and $\overline{\rho}_0$ for both functions. For REE, a smooth transition is introduced as σ_{th} approaches 0. Hence, REE is adopted as the threshold stress equation in the following sections.

Additionally, to account for the effect of work hardening in PCA on enhancing creep resistance with accumulated plastic strain when surpassing σ_{end} in loading stage, a weakening factor w, with a value less than 1.0 is introduced to influence the threshold stress variation in Eq. (4) for PCA and the equation becomes:

$$\begin{cases} \sigma_{th} = \sigma_{th_0} / (1 + \exp(n_{1a} (\overline{\rho}_{0i} + w \Delta \overline{\rho}_0)^{m_{1a}} - B) \\ \Delta \overline{\rho}_0 = \overline{\rho}_0 - \overline{\rho}_{0i} \end{cases} \tag{5}$$

where $\overline{\rho}_{0i}$ is the initial value of $\overline{\rho}_0$ for PCA, which is induced by pre-stretching ($\overline{\rho}_{0i} = 0$ for CA). $\Delta \overline{\rho}_0$ is the accumulated dislocation density in loading stage. For CA condition, as the diminishing of creep promotion was not observed, w can be defined as 1.0 and Eq. (5) then becomes equivalent to its original form of Eq. (4) adopted for CA.

4.1.3. Loading stage dislocation density determination with work hardening model

To calculate the threshold stress with proposed Eq. (5), the plastic strain ε_p and resultant dislocation density ρ_0 in the loading stage need be determined. The inducement of a non-linear stress-strain relationship is an indication of introducing plastic strain through work hardening. A form of Nadai model able to express stress-strain response in both elastic and work hardening regions was adopted to obtain the total strain induced in the loading stage as (Nádai and Wahl, 1931):

$$\boldsymbol{\varepsilon} = \begin{cases} \sigma/E \;\; \sigma \le \boldsymbol{\sigma_{end}} \\ \sigma/E + K(\boldsymbol{\sigma} - \boldsymbol{\sigma_{end}})^{n'} \;\; \sigma > \boldsymbol{\sigma_{end}} \end{cases} \tag{6}$$

where K and n' are material constants. When the applied stress σ surpasses σ_{end}, the plastic strain can be calculated by deducting the linear elastic strain as:

$$\varepsilon_p = \begin{cases} 0 \;\; \sigma \le \sigma_{end} \\ \dfrac{\sigma - \sigma_{end}}{E} + K(\sigma - \sigma_{end})^{n'} \;\; \sigma > \sigma_{end} \end{cases} \tag{7}$$

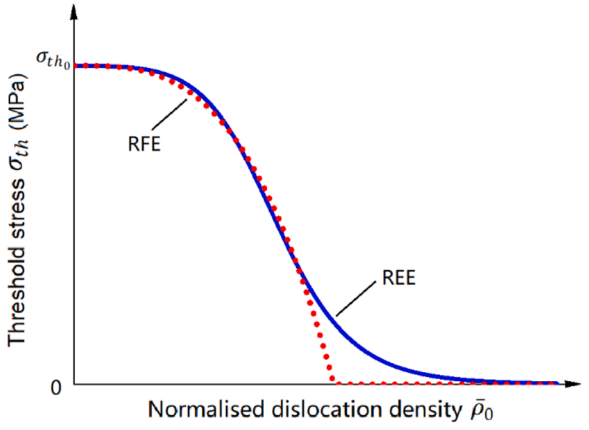

Fig. 9. Schematic of threshold stress σ_{th} variation with normalised dislocation density $\overline{\rho}_0$ for the ramp function equation (RFE, Eq. (3)) and the reversed exponential equation (REE, Eq. (4)), showing the sudden turn for the former and smooth transition for the latter when σ_{th} approaches zero.

With derived plastic strain in the loading stage, the dislocation density can be obtained through a widely adopted rate form dislocation density constitutive equation as (Lin et al., 2005):

$$\dot{\overline{\boldsymbol{\rho}}}_0 = \boldsymbol{A}_1(1-\overline{\boldsymbol{\rho}}_0)\left|\dot{\boldsymbol{\varepsilon}}_{\boldsymbol{p}}\right|^{\boldsymbol{m}_1} - \boldsymbol{C}_{\boldsymbol{p}}\overline{\boldsymbol{\rho}}_0^{\boldsymbol{m}_2} \tag{8}$$

where $\dot{\varepsilon}_p$ is the plastic strain rate which can be derived through the differentiation of Eq. (7) with regard to time; A_1, m_1, C_p and m_2 are material constants. The dynamic term $A_1(1-\overline{\rho}_0)|\dot{\varepsilon}_p|^{m_1}$ in Eq. (8) is the dislocation density variation due to creep deformation and dynamic recovery, $C_p\overline{\rho}_0{}^{m_2}$ is the static term accounted for the recovery of the dislocation at elevated temperature.

For PCA condition, the same expression of Eq. (7) is adopted to describe the relation between stress and plastic strain. However, as demonstrated in Fig. 5c, due to stronger work hardening induced by pre-stretching, another set of material constants K and n' in Eq. (7) needs to be fitted to model the observed less divergence from the linear stress-strain curve when surpassing σ_{end} for PCA. Additionally, considering that drastic microstructure evolution, like new grain boundary formation and recrystallisation, is unlikely to be induced with 3% pre-stretching (except for more dislocations) (Merriman and Field, 2012), the same material constants A_1, m_1, C_p and m_2 are adopted in Eq. (8) to calculate the plastic strain-induced dislocation density $\overline{\rho}_0$ in loading stage for PCA.

4.2. Microstructural constitutive equations

Creep can be viewed as time dependent plastic deformation, hence Eq. (8) is also applicable to express the evolution of creep strain-induced dislocation density in creep-ageing by substituting plastic strain ε_p with creep strain ε_{cr} as:

$$\dot{\overline{\boldsymbol{\rho}}} = \boldsymbol{A}_1(1-\overline{\boldsymbol{\rho}})\left|\dot{\boldsymbol{\varepsilon}}_{\boldsymbol{cr}}\right|^{\boldsymbol{m}_1} - \boldsymbol{C}_{\boldsymbol{p}}\overline{\boldsymbol{\rho}}^{\boldsymbol{m}_2} \tag{9}$$

where $\overline{\rho}$ is the normalised dislocation density with the same form of Eq. (3) as $\overline{\rho} = (\rho-\rho_i)/(\rho_m-\rho_i)$ and has a value range from 0 to 1. It should be noted that due to the pre-existing dislocation density $\overline{\rho}_0$ at the end of the loading stage, the value of dislocation density at the beginning of creep-ageing is $\overline{\rho} = \overline{\rho}_0$. Additionally, since the loading and creep-ageing stages are continuous and conducted at the same temperature, it is reasonable to adopt the same material constants A_1, m_1, C_p, and m_2 in Eq. (8) for Eq. (9).

A normalised precipitate size $\overline{r}$ is adopted to describe precipitate growth in creep-ageing, defined as:

$$\overline{r} = \frac{r}{r_0} \tag{10}$$

where r stands for the average precipitate radius and r_0 is the radius at the as-received T8 state. Thus, the initial value of the normalised precipitate size is 1. The as-received precipitate size r_0 is adopted to facilitate linking the simulation results with experimental data. For precipitate growth, a widely adopted growth rate equation is used (Zhan et al., 2011):

$$\dot{\overline{\boldsymbol{r}}} = \boldsymbol{C}_r(\boldsymbol{Q}-\overline{\boldsymbol{r}})^{\boldsymbol{m}_3}(1+\boldsymbol{\gamma}_0\overline{\boldsymbol{\rho}}^{\boldsymbol{m}_4}) \tag{11}$$

where Q represents the upper limit of precipitate growth during creep-ageing stage, at which a stable state is reached with the growth rate dropping to zero. C_r, m_3, γ_0, and m_4 are material constants. The observed strong stress-dependent characteristic of precipitate growth is accomplished by introducing the term $(1+\gamma_0\overline{\rho}^{m_4})$, expressing the acceleration of precipitation kinetics with higher dislocation density. The extent of the positive effect on precipitate growth caused by stress-induced dislocation density can be controlled through this term.

4.3. Strengthening constitutive equations

The phenomenon of dislocation hardening behaviour in creep-ageing is well recognised (Zhan et al., 2011; Zheng et al., 2018). The hardening behaviour is closely related to the dislocation density evolution induced by creep deformation. Additionally, in this study, the strength contribution of dislocation density generated in the loading stage is also considered by assuming $\overline{\rho} = \overline{\rho}_0$ at the beginning of creep-ageing stage. A well-established dislocation hardening (σ_{dis}) equation is adopted (Li et al., 2017; Zhan et al., 2011):

$$\dot{\boldsymbol{\sigma}}_{\boldsymbol{dis}} = \boldsymbol{A}_2\boldsymbol{n}_{\boldsymbol{d}}\overline{\boldsymbol{\rho}}^{\boldsymbol{n}_d-1}\dot{\overline{\boldsymbol{\rho}}} \tag{12}$$

where A_2 and n_d are material constants.

Precipitates are obstacles to dislocation movements during creep/plastic deformation. When a dislocation encounters precipitates during moving, two interaction mechanisms can happen based on the precipitate size: dislocation can shear through small precipitates or bypass large precipitate in the form of Orowan loop (Shercliff and Ashby, 1990). Hence precipitation hardening can be viewed as composed of two types of strengthening contributions, i.e. shearing strength σ_A, and bypassing strength σ_B, which have been given respectively as (Kelly and Nicholson, 1963)

$$\begin{aligned}\sigma_A &= c_1 f^{m_a} r^{n_a}\\ \sigma_B &= c_2 f^{m_b}/r^{n_b}\end{aligned} \tag{13}$$

Where f is the volume fraction of precipitates; c_1 and c_2 are material constants; m_a, n_a, m_b, and n_b are coefficients determining strength contributions from volume fraction and precipitate size. An approximation of cubic exponential relationship between

normalised volume fraction $\bar{f}$ and precipitate size r was proposed by Reti and Flemings (1972), and is adopted here:

$$\bar{f} = \frac{f}{f_s} = \frac{f}{f_0}\frac{f_0}{f_s} = \left(\frac{r}{r_0}\right)^3 \bar{f}_0 = \bar{r}^3 \bar{f}_0 \tag{14}$$

where f_s is the equilibrium volume fraction at ageing temperature, f_0 is the initial volume fraction at beginning of creep-ageing stage, $\bar{f}_0$ is the corresponding normalised volume fraction defined as $\bar{f}_0 = f_0/f_s$. By substituting Eq. (14) into Eq. (13) and utilising the derivation process used in a previous research (Li et al., 2017), equation for precipitate hardening in normalised form can be written as:

$$\begin{aligned} \sigma_A &= c'_1 \bar{r}^{m_{na}} \\ \sigma_B &= c'_2 / \bar{r}^{m_{nb}} \end{aligned} \tag{15}$$

where c'_1, c'_2, m_{na},and m_{nb} are material constants. From Eq. (15), it can be derived that when dislocation-precipitate interaction is dominated by shearing mechanism (σ_A), the precipitate hardening increases with precipitate growth. On the other hand, when the dominating mechanism changes to bypassing (σ_B), precipitate hardening decreases with the growth of precipitate. A harmonic function to combine the hardening effects generated by the two interaction mechanisms was proposed in Shercliff and Ashby (1990) as:

$$\sigma_{ppt} = \left({\sigma_A}^{-1} + {\sigma_B}^{-1}\right)^{-1} \tag{16}$$

where σ_{ppt} is the overall precipitation hardening combining strength contribution of shearing (σ_A) and bypassing (σ_B) mechanisms. When $\sigma_A = \sigma_B$, the change of interaction mechanisms from shear to bypassing happens, indicating the start of over-aged state.

The overall yield strength evolution can be considered as composed of hardening effects caused by different mechanisms, such as dislocation and precipitation hardening. An addition law is adopted to express the evolution of yield strength σ_y as:

$$\sigma_y = \sigma_i + \left({\sigma_{ppt}}^{n_y} + {\sigma_{dis}}^{n_y}\right)^{1/n_y} \tag{17}$$

where σ_i is the intrinsic strength including solid solution hardening of the alloy, n_y is an exponent constant to control the relative strength contribution of precipitation and dislocation hardening, which was assigned with value of 2 in Ma et al. (2018) and varies with precipitate thickness in Li et al. (2019). In this study, n_y was determined in the range of 1 to 2 as suggested by Fribourg et al. (2011).

Table 4
Unified constitutive model including work hardening.

Work hardening sub-model	**Microstructure variables**
$\varepsilon_p = (\sigma - \sigma_{end})/E + K(\sigma - \sigma_{end})^{n'}$ $\dot{\bar{\rho}}_0 = A_1(1-\bar{\rho}_0)\lvert\dot{\varepsilon}_p\rvert^{m_1} - C_p\bar{\rho}_0^{m_2}$ $\sigma_{th} = \sigma_{th_0}/(1+\exp(n_{1a}(\bar{\rho}_{0i} + w\Delta\bar{\rho}_0)^{m_{1a}} - B)$	$\dot{\bar{\rho}} = A_1(1-\bar{\rho})\lvert\dot{\varepsilon}_{cr}\rvert^{m_1} - C_p\bar{\rho}^{m_2}$ $\dot{\bar{r}} = C_r(Q-\bar{r})^{m_3}(1+\gamma_0\bar{\rho}^{m_4})$
Stress-creep strain relationship	**Strengthening equations**
$\dot{\varepsilon}_{cr} = A_3\sinh(B_1(\sigma-\sigma_{th})(1-H)^{n_2})(1+k_3\bar{\rho}_{0i}/(k_4\varepsilon)^{n_3})$ $H = k_1(\bar{\rho}-\bar{\rho}_0) + k_2\bar{r}$	$\dot{\sigma}_{dis} = A_2 n_d \bar{\rho}^{n_d-1}\dot{\bar{\rho}}$ $\dot{\sigma}_{dis} = A_2 n_d \bar{\rho}^{n_d-1}\dot{\bar{\rho}}$ $\sigma_{ppt} = (\sigma_A^{-1} + \sigma_B^{-1})^{-1}$ $\sigma_y = \sigma_i + (\sigma_{ppt}^{n_y} + \sigma_{dis}^{n_y})^{1/n_y}$
Parameters in work hardening sub-model	
ε_p: plastic strain induced in loading stage $\bar{\rho}_0$: normalised dislocation density in loading $\bar{\rho}_{0i}$: initial dislocation density induced by pre-stretching for PCA $\Delta\bar{\rho}_0$: accumulated dislocation density in loading	σ_{end}: stress at the end of linear stress-strain relation σ_{th}: threshold stress σ_{th_0}: initial threshold stress E, K, n', A_1, m_1, C_p,m_2, n_{1a}, w, m_{1a}, B: are material constants
Parameters for microstructure variable	
$\bar{\rho}$: normalised dislocation density in creep-ageing $\bar{r}$: normalised precipitate size	ε_{cr}: creep strain A_1, m_1, C_p,m_2, C_r, Q, m_3, γ_0, m_4 are material constants
Parameters in stress-creep strain relationship	
ε: strain accumulated in loading H: creep variable	A_3, B_1, n_2, k_3, k_4, n_3, k_1, k_2 are material constants
Parameters in strengthening equations	
σ_{dis}: dislocation hardening σ_A: strengthening by dislocation cutting through precipitate σ_i: material intrinsic strength	σ_{ppt} : precipitation hardening σ_B: strengthening by dislocation bypassing precipitate A_2, n_d, n_y are material constants

4.4. Stress-creep strain relationship

The classical sinh-law equation is adopted to link the creep strain rate $\dot{\varepsilon}_{cr}$ with the applied stress in creep-ageing stage. To account for the decrease of creep strain rate caused by material hardening induced by microstructural evolution during creep-ageing, a creep variable H is introduced, representing the effects of normalised dislocation density $\overline{\rho}$ and precipitate size $\overline{r}$ (Ho et al., 2004a; Li et al., 2017). In this study, considering the effect of threshold stress, the group of constitutive equations to express stress-creep strain relationship is given as:

$$\begin{cases} \dot{\varepsilon}_{cr} = A_3 \sinh(B_1(\sigma - \sigma_{th})(1-H)^{n_2}) \\ H = k_1(\overline{\rho} - \overline{\rho}_0) + k_2\overline{r} \end{cases} \tag{18}$$

where A_3 and B_1 are material constants. n_2 is an exponent constant controlling the effect of creep variable H.

Earlier analysis shows that creep deformation in PCA is promoted due to increased mobile dislocation induced by pre-stretching, while this promotion effect is diminishing with increased work hardening. To adequately reflect the observed dynamic evolution trend of creep deformation for PCA, Eq. (18) can be modified as:

$$\begin{cases} \dot{\varepsilon}_{cr} = A_3 \sinh(B_1(\sigma - \sigma_{th})(1-H)^{n_2})(1 + k_3\overline{\rho}_{0i}/(k_4\varepsilon)^{n_3}) \\ H = k_1(\overline{\rho} - \overline{\rho}_0) + k_2\overline{r} \end{cases} \tag{19}$$

where ε is the strain generated in the loading stage as shown in Eq. (6). k_3, k_4 and n_3 are material constants. In the supplement factor $(1 + k_3\overline{\rho}_{0i}/(k_4\varepsilon)^{n_3})$, $k_3\overline{\rho}_{0i}$ is introduced to account for the promotion of creep deformation due to pre-stretching-induced mobile dislocation, similar to a previous study (Yang et al., 2017); while $(k_4\varepsilon)^{n_3}$ reflects the diminishing of the deformation promotion with increased work hardening for PCA. It should be noted that without pre-stretching, i.e. for CA case, $\overline{\rho}_{0i}$ equals zero and the factor $(1 + k_3\overline{\rho}_{0i}/(k_4\varepsilon)^{n_3})$ becomes 1, hence Eq. (19) reverts to Eq. (18).

By combining the proposed equations above, a unified constitutive model is presented in Table 4. Through the work hardening sub-model, the plastic strain and plastic strain-induced dislocation density in the loading stage can be determined, with which the threshold stress at the beginning of creep-ageing stage is obtained. With the expression of microstructure variables in creep-ageing, the creep deformation behaviour and material strength evolution can be modelled with the proposed corresponding constitutive equations for both CA and PCA.

5. Model calibration, results and discussion

5.1. Determination of initial values and material constants

Since the constitutive equations are ordinary differential equations (ODE) requiring initial values to solve, adopting reasonable initial values for internal variables in the constitutive model is significant for its establishment. These values include initial strength hardening contribution of dislocation density σ_{dis0}, precipitation hardening σ_{ppt0}, and intrinsic strength σ_i. To determine the initial values of these strength components, a SHT and pre-stretching method was adopted as demonstrated in Fig. 10. σ_i is defined to be equal to SHTed yield strength σ_{y1}. σ_{dis0} can be approximated as the difference between the SHTed yield strength σ_{y1} and the 3% pre-stretched yield strength σ_{y2}, as shown in the figure. σ_{ppt0} can be calculated through Eq. (17). The initial value of $\overline{\rho}_0$ induced by pre-stretching for PCA, i.e. $\overline{\rho}_{0i}$, is determined from the REE curve for the relationship between threshold stress and normalised dislocation density which will be further illustrated in Section 5.2. The remaining variables can be determined directly from experimental data or assigned with initial values as defined. The initial values for the material in this study are listed in Table 5.

The proposed constitutive model is composed of groups of non-linear ODEs that cannot be solved analytically. In this study, the

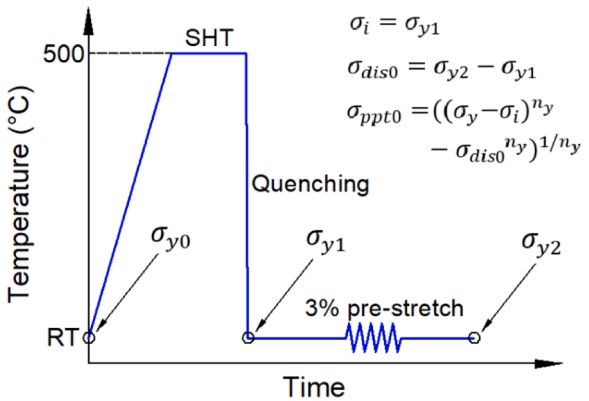

Fig. 10. Schematic of the thermal history and the determination method for initial values of strength components. RT stands for room temperature.

Table 5
Determined initial values for the constitutive model.

$\overline{\rho}_0$ for CA	$\overline{\rho}_0$ for PCA ($\overline{\rho}_{0i}$)	ε_p	$\overline{r}$	σ_{end} (MPa)
0	3.74E-2	0	1	396
σ_{th0} (MPa)	$\sigma_{tho}^{'}$ (MPa)	σ_i (MPa)	σ_{dis0} (MPa)	σ_{ppt0} (MPa)
105	85	299	56	140.2

forward Euler method was adopted to solve the equations:

$$s_{n+1} = s_n + \dot{s}_n \Delta t \tag{20}$$

where s_{n+1} and s_n are values of internal variable s at time step n+1 and n respectively; $\dot{s}_n$ is the evolution rate at time step n; Δt is the time increment. With the derivation of approximate solutions of internal variables, the least square method is adopted to determine the material constants that allow the model to be best fitted with experimental data, i.e. with the minimum value of an objective function. The objective function is written as

$$f(x) = \sum_{i=1}^{L2} \sum_{j=1}^{L3} \left(y_{ij}^{m} - y_{ij}^{e} \right)^2 \tag{21}$$

where $x = (x_1, x_2, x_3, \ldots, x_{L1})$ is the material parameters with a total number of $L1$ to be determined in the model. $L2$ is the number of series classified by different applied stresses, $L3$ is the number of data points in each series. y_{ij}^{m} and y_{ij}^{e} stand for the i-th stress series and j-th data point of the model-derived value and experimental value respectively. The determined material constants are listed in Table 6. In this study, the experimental data of 422.5 MPa for both CA and PCA were used for verification only and not used in the determination of material constants.

5.2. Modelling results and discussion

5.2.1. Work hardening model

The stress-strain curves in the loading stage to 430 MPa, as predicted by Eq. (7), are shown as red dashed lines in Figs. 4b and 5c, respectively for CA and PCA cases, demonstrating a close match with the experimental results. The plastic strain was induced when the linear stress-strain relationship broke down in the loading stage. Therefore, the normalised dislocation density at the end of loading stage can be calculated from Eq. (8). The plastic strain and corresponding normalised dislocation densities at the end of the loading stage are shown as the solid and dashed curves for CA and PCA respectively in Fig. 11a. Similar evolution trend can be observed for both cases and $\overline{\rho}_0$ increases with plastic strain ε_p.

With the obtained $\overline{\rho}_0$ values at the end of the loading stage, the threshold stresses for CA can be calculated with the proposed REE Eq. (5) and are shown as the solid curve in Fig. 11b, in which the corresponding applied stresses are indicated. As can be observed for CA, threshold stress maintains at a relative high value at the beginning (i.e. lower stress level) and drops sharply with an increasing rate as the applied stress and the accumulated dislocation density increase. When the threshold stress approaches zero, a smooth transition is shown with REE. The dramatic drop of threshold stress with the induced plastic strain/dislocation density in the loading stage can lead to the nonlinear increase of the stress $(\sigma - \sigma_{\text{th}})$ against the applied stress σ.

Fig. 11b also shows the threshold stress variation with dislocation density for PCA (dashed line), calculated with the proposed REE Eq. (5). With the determination of the $\sigma_{tho}^{'}$ value for PCA, the corresponding initial value of dislocation density induced by pre-stretching, $\overline{\rho}_{0i}$, can be determined from the REE curve as illustrated by the dotted lines in Fig. 11b. Due to stronger work hardening effect induced by pre-stretching, the threshold stress of PCA drops much slower with increasing stress and dislocation density when compared with CA.

Table 6
Determined material constants for the proposed constitutive model.

A_1 (h^{-1})	A_2 (MPa)	A_3 (h^{-1})	B	B_1 (MPa^{-1})	$c_1^{'}$	$c_2^{'}$
26	14	8.43E-8	10.5	3.6E-2	225	365
C_p	C_r (h^{-1})	E (MPa)	K for CA (MPa^{-1})	K for PCA (MPa^{-1})	k_1	k_2
6.5E-3	8E-2	6.26E4	9.36E-8	6.67E-8	0.5	5.2E-2
k_3	k_4	m_1	m_{1a}	m_2	m_3	m_4
1.1E-2	100	5.42E-1	0.52	0.75	1.05	1.5
m_{na}	m_{nb}	$n^{'}$ for CA	$n^{'}$ for PCA	n_{1a}	n_2	n_3
0.83	0.03	2.35	2.25	50	1.28	8.6
n_d	n_y	Q	w	γ_0		
4.2	1.16	1.52	0.12	8		

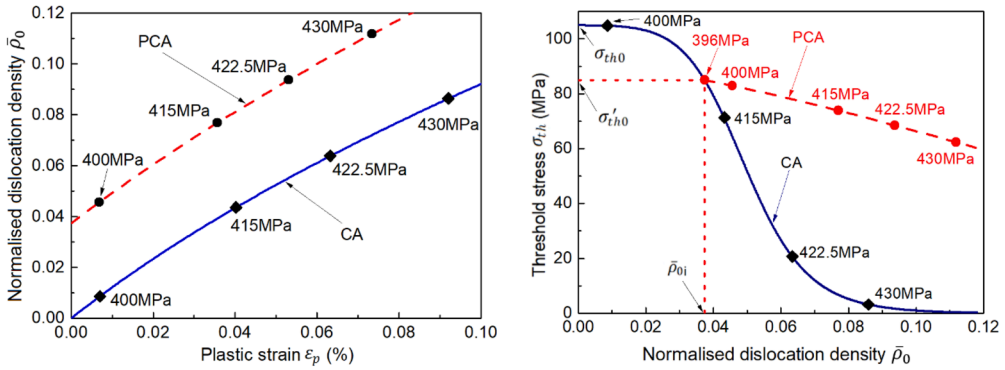

(a) $\bar{\rho}_0$ versus ε_p (b) σ_{th} versus $\bar{\rho}_0$

Fig. 11. Relationship among the plastic strain, normalised dislocation density and threshold stress at the end of loading stage, showing higher normalised dislocation density during loading for PCA in (a) and faster decrease of threshold stress above 400 MPa for CA in (b). (a) $\bar{\rho}_0$ versus ε_p; (b) σ_{th} versus $\bar{\rho}_0$.

5.2.2. *Stress-creep strain relationship*

Fig. 12a compares the modelled creep strain curves with the experimental data under different stresses for CA. The modelled creep strain curves fit very well with the data. The distinct 6 times increase of creep strain when the applied stress increases from 400 to 430 MPa has been adequately reflected in the model. This nonlinear increase in creep strain can be attributed to the higher initial plastic strain and dislocation density being generated in the loading stage with higher stress, causing a dramatic decrease of the threshold stress within the applied stress ranging from 400 to 430 MPa as shown in Fig. 11b. The 422.5 MPa results were not used for determining material constants, and the good agreement with the model prediction verifies the adequacy of the proposed model.

Fig. 12b demonstrates the fitting results for creep strain curves of PCA. By considering the promotion of creep deformation caused by pre-stretching-induced dislocations and its diminishing due to increased work hardening, the creep strain evolution for PCA condition under different stresses is adequately modelled. As observed from Fig. 12b, the modelling results are in close agreement with the experimental data. Again, the results from 422.5 MPa were not used in the determination of material constants and therefore the close match validates the model applicability. For stresses below 400 MPa, a much lower creep strain increment per unit stress was obtained when compared with that above 400 MPa as demonstrated in Fig. 5d. In the meantime, the sinh-law used for the stress-creep strain relationship is suitable to a wider range of stress levels (Lin, 2003). As a result, it is expected that the fitting stresses of 300, 360, and 400 MPa are adequate to guarantee the prediction accuracy below 400 MPa. Additionally, this constitutive model is unified for both CA and PCA conditions, where $\bar{\rho}_{0i}$ and w respectively equal to zero and 1.0 for CA condition. It is noticed that minor deviations exist between the simulation and experimental results with lower applied stresses for CA and PCA (300 MPa to 400 MPa), however the overall results are acceptable as the maximum creep strain error is only 0.008% for 360 MPa PCA.

5.2.3. *Microstructural evolution*

Fig. 13 shows the comparison of fitting results with normalised experiment data for dislocation density and precipitate size during creep-ageing for CA. As shown in Fig. 13a, the dislocation density evolution under different stresses is reflected by the model (a ρ_m

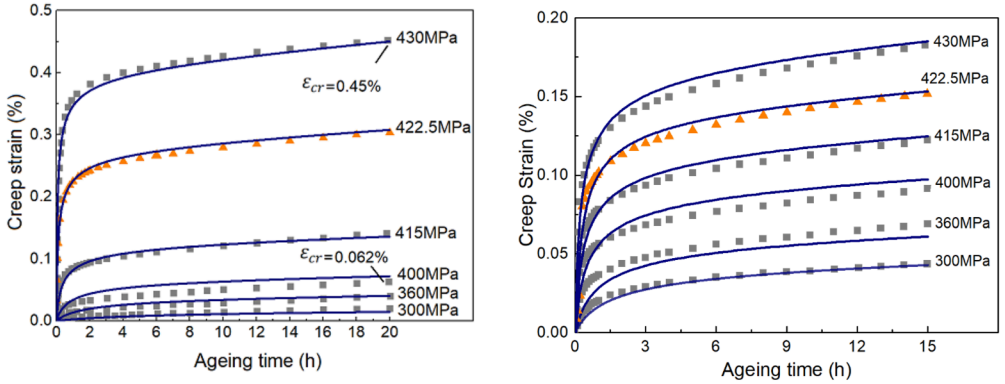

(a) As-received material (b) Pre-stretched material

Fig. 12. Comparison of modelled (lines) and experimental (symbols) creep strain evolutions of the as-received and the pre-stretched materials under indicated stress levels. The triangle symbols are data used for verification. (a) As-received material; (b) Pre-stretched material.

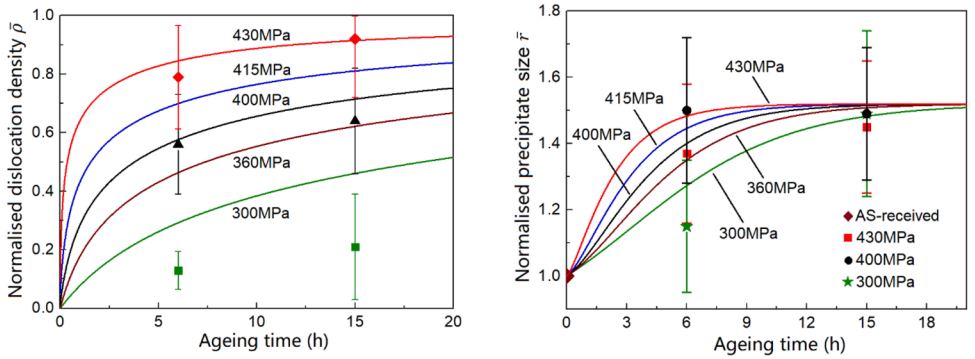

(a) Dislocation density evolution (b) Precipitate size evolution

Fig. 13. Comparison of modelled (lines) and experimental (symbols) evolutions of the normalised dislocation density and normalised precipitate size with ageing time in the as-received material under the indicated applied stress levels. (a) Normalised dislocation density; (b) Normalised precipitate size.

value of 6.8×10^{13} m^{-2} was determined by fitting with the experimental data and simulation results using $\overline{\rho} = (\rho - \rho_i)/(\rho_m - \rho_i)$). It can be noticed that under all stresses, the dislocation density increases at a higher rate in the initial hours in which fast creep strain increase is obtained and then increases at gradually reduced rates afterwards. Additionally, discrepancies are observed with the dislocation density under 300 MPa. This can be caused by the term $(1-\overline{\rho})$ adopted in Eq. (9), which may overestimate the dislocation increase rate when the value of $\overline{\rho}$ is low. Fig. 13b shows the precipitate size evolution under different stresses, which generally increases quickly and then comes to a plateau. Dislocation-enhanced precipitate growth can be observed from the modelling curves that the size growth rate of 430 and 400 MPa is higher than the 300 MPa. Similarly, a higher precipitate size is observed in the simulation results with lower stress of 300 MPa at 6 h which can be attributed to the overestimation of dislocation density $\overline{\rho}$ with lower stress. There are also differences between the model and experimental results for the precipitate size under 400 and 430 MPa. However, the predicted curves of precipitate size evolution with the three selected stresses fall into the error range of corresponding experiment data, indicating the model's ability to reflect the stress dependency effect on microstructure evolutions in creep-ageing.

5.2.4. Strength evolution

Fig. 14 presents the evolution of yield strength and strength contribution of corresponding hardening mechanisms during creep-ageing for CA. The yield strength evolution in creep-ageing under 300, 400 and 430 MPa are demonstrated in Fig. 14a. A rising trend can be seen under all stresses during creep-ageing. It can be observed that higher material strength is obtained with higher applied stress in creep-ageing due to the effects of precipitation and dislocation hardening. Fig. 14b schematically illustrates the strength contribution by different hardening effects under 400 MPa, including intrinsic strength, precipitation hardening, and dislocation hardening. Since the creep age hardening results in around 30 MPa increase of the yield strength while a 3% pre-stretch (the stretching is much more than the creep strain) leads to 15 MPa increase, the yield strength increase can be assumed to be more associated with precipitation hardening than dislocation hardening, consistent with the assumptions in previous studies (Rong et al., 2021; Zheng et al., 2018). It should be noted that solid solution hardening is included in the intrinsic strength which is not expected to change significantly as the as-received material was in T8 temper.

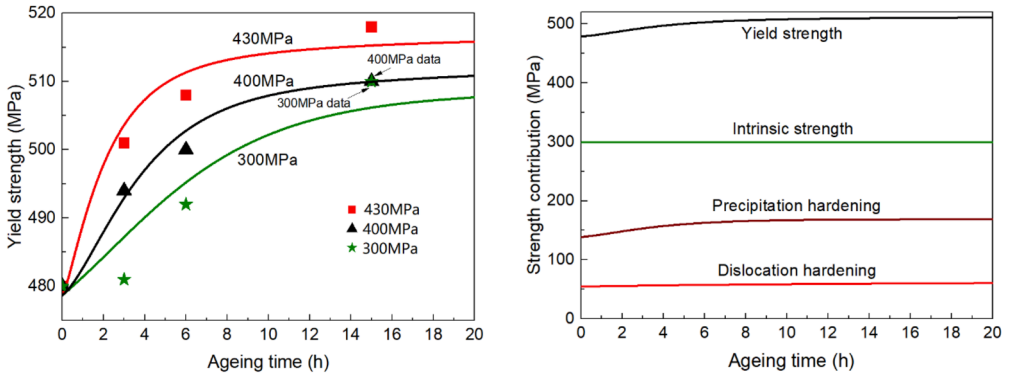

(a) Yield strength evolution (b) Strength contribution under 400 MPa

Fig. 14. Evolution of the yield strength and strength contributions with ageing time for the as-received material. The experimental results are marked with symbols and modelling with lines. (a) Yield strength evolution; (b) Strength contribution under 400 MPa.

5.3. Model extension to the multiaxial case

5.3.1. Extension to multiaxial case

In this section, the proposed and determined material model will first be transformed to the multiaxial form and then applied to a four-point bending CAF case. Assuming the material follows von-Misese behaviour with isotropic hardening, the applied uniaxial stress σ in the rolling direction is replaced by the equivalent stress $\widetilde{\sigma}_{vm}$ in the multiaxial case as $\widetilde{\sigma}_{vm} = (3S_{ij}S_{ij}/2)^{1/2}$, where $S_{ij} = \sigma_{ij} - \delta_{ij}\sigma_{kk}/3$ is the deviatoric stress of the ij component. The work hardening model for the multiaxial case can be expressed in terms of equivalent stress $\widetilde{\sigma}_{vm}$ and equivalent strain $\widetilde{\varepsilon}$ as

$$\widetilde{\varepsilon} = \begin{cases} \widetilde{\sigma}_{vm}/E & \widetilde{\sigma}_{vm} \le \sigma_{end} \\ \dfrac{\widetilde{\sigma}_{vm}}{E} + K(\widetilde{\sigma}_{vm} - \sigma_{end})^{n'} & \widetilde{\sigma}_{vm} > \sigma_{end} \end{cases} \tag{22}$$

where $\widetilde{\varepsilon}$ is a scalar to reflect the deformation in the multiaxial case during the loading stage. Accordingly, both the equivalent plastic strain $\widetilde{\varepsilon}_p$ and the normalised dislocation density $\overline{\rho}_0$ accumulated in the loading stage can be derived as

$$\begin{cases} \widetilde{\varepsilon}_p = 0 & \widetilde{\sigma}_{vm} \le \sigma_{end} \\ \widetilde{\varepsilon}_p = \dfrac{\widetilde{\sigma}_{vm} - \sigma_{end}}{E} + K(\widetilde{\sigma}_{vm} - \sigma_{end})^{n'} & \widetilde{\sigma}_{vm} > \sigma_{end} \\ \dot{\overline{\rho}}_0 = A_1(1-\overline{\rho}_0)\left|\dot{\widetilde{\varepsilon}}_p\right|^{m_1} - C_p\overline{\rho}_0^{m_2} & \end{cases} \tag{23}$$

Assuming normality associated flow rule, the uniaxial model can be extended to apply in the multiaxial case, following the extension method proposed in (Ho et al., 2004b) as

$$\begin{cases} \dot{\widetilde{\varepsilon}}_{cr} = A_3\sinh(B_1(\widetilde{\sigma}_{vm} - \sigma_{th})(1-H)^{n_2})\left(1 + \dfrac{k_3\overline{\rho}_{0i}}{(k_4\widetilde{\varepsilon})^{n_3}}\right) \\ H = k_1(\overline{\rho} - \overline{\rho}_0) + k_2\overline{r} \\ \sigma_{th} = \sigma_{th_0}/(1 + \exp(n_{1a}(\overline{\rho}_{0i} + w\Delta\overline{\rho}_0)^{m_{1a}} - B) \\ \dot{\overline{\rho}} = A_1(1-\overline{\rho})|\dot{\widetilde{\varepsilon}}_{cr}|^{m_1} - C_p\overline{\rho}^{m_2} \\ \dot{\overline{r}} = C_r(Q - \overline{r})^{m_3}(1 + \gamma_0\overline{\rho}^{m_4}) \\ D_{ij}^p = \left(3S_{ij}/(2\widetilde{\sigma}_{vm})\right)\dot{\widetilde{\varepsilon}}_{cr} \end{cases} \tag{24}$$

where $\dot{\widetilde{\varepsilon}}_{cr}$ is the equivalent creep strain rate in the multiaxial case, D_{ij}^p is the rate of plastic deformation.

Since the work hardening model is proposed to reflect the deviation from linear stress-strain relation with small deformation in the loading stage, the plasticity behaviour of the material in the loading stage can be assumed as path independent (Dougill, 1975), i.e. the same stress-strain relation (Eq. (22)) and dislocation density evolution with the induced plastic strain (Eq. (23)) is followed respectively. Hence the model can be used to predict creep-ageing behaviour with proportional and non-proportional loading as (Ho et al., 2004b):

$$\begin{cases} D_{ij}^e = D_{ij}^T - D_{ij}^P \\ \widehat{\sigma}_{ij} = GD_{ij}^e + 2\lambda D_{kk}^e \end{cases} \tag{25}$$

where D_{ij}^e and D_{ij}^T are respectively the rates of elastic deformation and total deformation. $\widehat{\sigma}_{ij}$ is the Jaumann rate of Cauchy stress. G and λ are the Lamé constants.

5.3.2. Model application to four-point bending CAF

For model application to an actual case, a finite element (FE) model was established in ABAQUS based on the dimensions of the specimens and bending tool, as shown in Fig. 15a. The loading cylinders were assigned with boundary conditions to allow them only moving in Y direction, while the support cylinders were completely fixed. The specimen was composed of four-node bilinear plane stress reduced integration shell elements (CPS4R) with a size of 0.2 mm x 0.2 mm for all thicknesses. The four cylinders were composed of discrete rigid elements with a size of 0.5 mm x 0.5 mm. The contacts between the loading cylinders and specimen, and between the specimen and supporting cylinders were modelled with tangential behaviour adopting penalty formulation with friction coefficient of 0.25. The proposed constitutive model was implemented in the FE software with VUMAT subroutine. Fig. 15b demonstrates the obtained simulation results for the 4 mm plate. It can be noticed that most of the creep strain was induced between the two loading cylinders, where the largest moment and stress were generated in the four-point bending tests. The comparison of experiment and simulation results for the deflections at the centre of the specimen after unloading is shown in Fig. 15c. As can be seen in the figure, good agreements were achieved between the simulation and experiment results with the maximum prediction error of 0.18 mm for the 6 mm thickness.

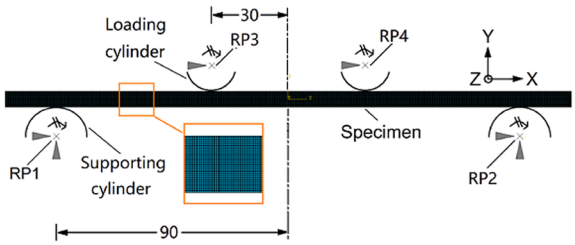

(a) Schematic of FE model (dimension in mm)

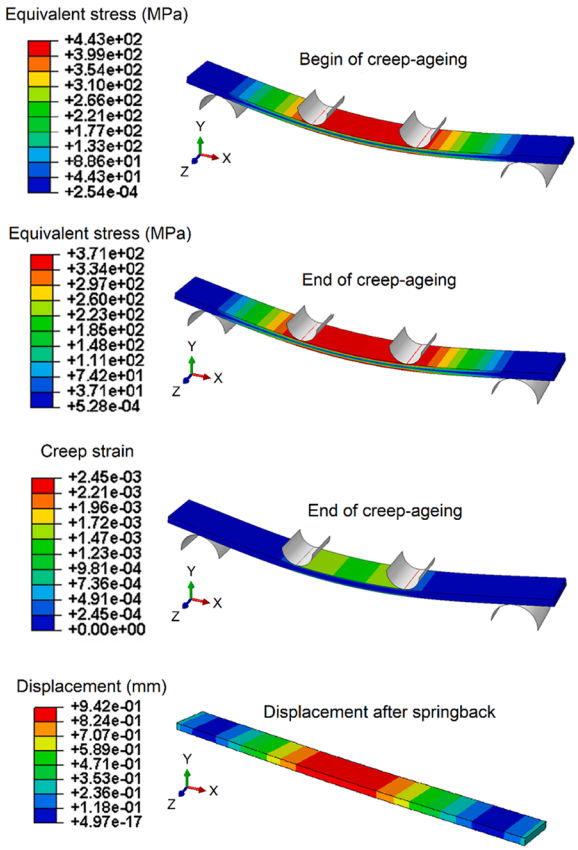

(b) Simulation results of 4 mm plate

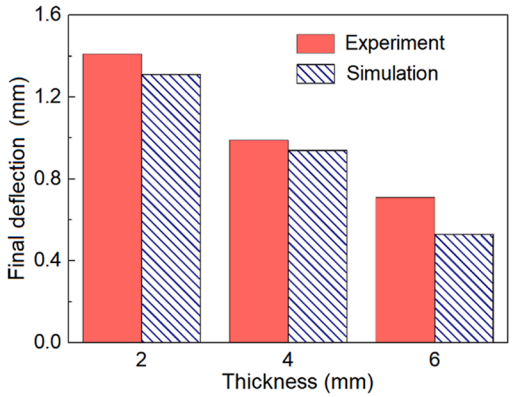

(c) Comparison of the final deflection results between experiments and simulations

(caption on next page)

Fig. 15. Demonstration of the four-point bending CAF numerical simulation and results. . (a) Schematic of FE model (dimension in mm); (b) Simulation results for 4 mm plate; (c) Comparison of the final deflections at the specimen centre after unloading between experiments and simulations.

6. Conclusions

In this paper, increasing creep strain of high strength Al-Li alloy has been investigated by inducing a small amount of plastic strain in the loading stage and by conducting 3% pre-stretching before creep-ageing. A unified mechanism-based constitutive model adequate to reflect the stress-creep strain relation with both conditions has been established. The following conclusions can be achieved:

1 Introducing plastic strain in loading stage or conducting 3% pre-stretching can improve the creep behaviour and mitigate the forming difficulty of the 3rd generation Al-Li alloy in CAF. The two routines are suitable for different ranges of applied stresses. For the former, more than 6 times increase of creep strain has been achieved when the applied stress increases from 400 to 430 MPa for CA. For the latter, the creep deformation has been enhanced in lower stresses ranging from 300 to 400 MPa with the PCAS to CAS ratio at 15 h ranging from 2.7 to 1.6. The enhancement of creep deformation is attributed to the effect of pre-induced dislocation on the reduction of threshold stress for both routines.
2 The promotion of creep deformation of the pre-stretched has been observed to be diminishing with the increase of the applied stress. When the applied stress is above 415 MPa, the 15 h creep strain of the pre-stretched is surpassed by the non-stretched, with continued dropping PCAS to CAS ratio lower than one. This diminishing of the creep deformation promotion can be attributed to the stronger work hardening induced at higher applied stress for the pre-stretched material.
3 A mechanism-based unified constitutive model combining work hardening equations has been proposed to describe the wide range of creep deformation of T8 tempered Al-Li alloy from 0.02% to 0.45% with corresponding applied stresses ranging from 300 to 430 MPa. Consistent results have been achieved between experimental and modelling results for macro creep-ageing behaviour and microstructural evolutions in aspects of dislocation and precipitation of material in loading and creep-ageing stages.
4 The proposed unified creep-ageing model can be applied to both the as-received material and the pre-stretched material. A supplement factor to account for the effect of pre-stretching-induced dislocation on creep deformation and a weakening factor for the effect of increased work hardening on diminishing creep promotion at higher applied stress are adopted for PCA condition, both of which become 1 for the CA case.
5 The adaptability of the proposed model to multiaxial condition has been well demonstrated by implementing its multiaxial form in the FE simulation for four-point bending CAF tests, with the maximum prediction error of 0.18 mm at the centre of the specimen after unloading.

CRediT authorship contribution statement

Xi Wang: Investigation, Methodology, Validation, Writing – original draft. **Qi Rong:** Writing – review & editing. **Zhusheng Shi:** Conceptualization, Funding acquisition, Supervision, Writing – review & editing. **Jianguo Lin:** Conceptualization, Writing – review & editing.

Declaration of Competing Interest

The authors declare that they have no known competing financial interests or personal relationships that could have appeared to influence the work reported in this paper.

Data availability

Data will be made available on request.

Acknowledgements

Financial support (grant number MESM_PSG110) from Commercial Aircraft Corporation of China (COMAC) is gratefully acknowledged.

References

Andrade, E, 1910. On the viscous flow in metals, and allied phenomena. Proc. R. Soc. Lond. A 84, 1–12.
Basirat, M, Shrestha, T, Potirniche, GP, Charit, I, Rink, K, 2012. A study of the creep behavior of modified 9Cr–1Mo steel using continuum-damage modeling. Int. J. Plast. 37, 95–107.
Brandon, B, Markus, H, Gary, B, Edward, C, Jeffrey, W, 2012. Advanced aluminum and aluminum-lithium solutions for derivative and next Generation aerospace structures. In: SAE 2012 AMAF Conference & Exhibition.
Chokshi, A, 2008. Diffusion creep in metals and ceramics: extension to nanocrystals. Mater. Sci. Eng. A 483-484, 485–491.

Chung, TF, Yang, YL, Hsiao, CN, Li, WC, Huang, BM, Tsao, CS, Shi, Z, Lin, J, Fischione, P, Ohmura, T, Yang, JR, 2018. Morphological evolution of GP zones and nanometer-sized precipitates in the AA2050 aluminium alloy. Int. J. Lightw. Mater. Manuf. 1, 142–156.
Dai, R, Deng, K, Wang, C, Nie, K, Zhang, G, Liang, W, 2022. Effects of precipitates and solute atoms on the work hardening and softening behavior of Zn-rich aluminum alloy. Mater. Sci. Eng. A 848, 143388.
Dorin, T, De, Geuser F, Lefebvre, W, Sigli, C, Deschamps, A, 2014. Strengthening mechanisms of T1 precipitates and their influence on the plasticity of an Al–Cu–Li alloy. Mater. Sci. Eng. A 605, 119–126.
Dougill, JW, 1975. Some remarks on path independence in the small in plasticity. Q. Appl. Math. 33, 233–243.
Dunand, DC, Jansen, AM, 1997. Creep of metals containing high volume fractions of unshearable dispersoids - part I. Modeling the effect of dislocation pile-ups upon the detachment threshold stress. Acta Mater. 45, 4569–4581.
Farrokh, B, Khan, A, 2009. Grain size, strain rate, and temperature dependence of flow stress in ultra-fine grained and nanocrystalline Cu and Al: synthesis, experiment, and constitutive modeling. Int. J. Plast. 25, 715–732.
Fribourg, G, Brechet, Y, Deschamps, A, Simar, A, 2011. Microstructure-based modelling of isotropic and kinematicstrain hardening in a precipitation-hardened aluminium alloy. Acta Mater. 59, 3621–3635.
Ho, KC, Lin, J, Dean, TA, 2004a. Constitutive modelling of primary creep for age forming an aluminium alloy. J. Mater. Process. Technol. 153-154, 122–127.
Ho, KC, Lin, J, Dean, TA, 2004b. Modelling of springback in creep forming thick aluminum sheets. Int. J. Plast. 20, 733–751.
Holman, MC, 1989. Autoclave age forming large aluminum aircraft panels. J. Mech. Work. Technol. 20, 477–488.
Hu, L, Zhan, L, Liu, Z, Shen, R, Yang, Y, Ma, Z, Liu, M, Liu, J, Wang, X, 2017. The effects of pre-deformation on the creep aging behavior and mechanical properties of Al-Li-S4 alloys. Mater. Sci. Eng. A 703, 496–502.
Kassner, ME, 2017. Fundamentals of creep in metals and alloys, third Edition. Zhong Nan Da Xue Chu Ban She.
Kelly, A, Nicholson, RB, 1963. Precipitation hardening. Prog. Mater. Sci. 10, 149–391.
Krempl, E, Khan, F, 2003. Rate (time)-dependent deformation behavior: an overview of some properties of metals and solid polymers. Int. J. Plast. 19, 1069–1095.
Krug, M, Dunand, DC, 2011. Modeling the creep threshold stress due to climb of a dislocation in the stress field of a misfitting precipitate. Acta Mater. 59, 5125–5134.
Lavrentev, F, 1980. The type of dislocation interaction as the factor determining work hardening. Mater. Sci. Eng. 46, 191–208.
Li, Y, Shi, Z, Lin, J, 2019. Experimental investigation and modelling of yield strength and work hardening behaviour of artificially aged Al-Cu-Li alloy. Mater. Des. 183, 108121.
Li, Y, Shi, Z, Lin, J, Yang, YL, Rong, Q, Huang, BM, Chung, TF, Tsao, CS, Yang, JR, Balint, DS, 2017. A unified constitutive model for asymmetric tension and compression creep-ageing behaviour of naturally aged Al-Cu-Li alloy. Int. J. Plast. 89, 130–149.
Lin, J, 2003. Selection of material models for predicting necking in superplastic forming. Int. J. Plast. 19, 469–481.
Lin, J, Liu, Y, Farrugia, D, Zhou, M, 2005. Development of dislocation-based unified material model for simulating microstructure evolution in multipass hot rolling. Philos. Mag. 85, 1967–1987.
Liu, C, Yang, J, Ma, P, Ma, Z, Zhan, L, Chen, K, Huang, M, Li, J, Li, Z, 2020. Large creep formability and strength–ductility synergy enabled by engineering dislocations in aluminum alloys. Int. J. Plast. 134, 102774.
Ma, Z, Zhan, L, Liu, C, Xu, L, Xu, Y, Ma, P, Li, J, 2018. Stress-level-dependency and bimodal precipitation behaviors during creep ageing of Al-Cu alloy: experiments and modeling. Int. J. Plast. 110, 183–201.
Merriman, C, Field, D, 2012. Observations of dislocation structure in AA 7050 by EBSD. Textures of materials - ICOTOM 16. Trans Tech Publications Ltd, pp. 493–498.
Mordehai, D, Clouet, E, Fivel, M, Verdier, M, 2008. Introducing dislocation climb by bulk diffusion in discrete dislocation dynamics. Philos. Mag. 88, 899–925.
Muñoz, MA, Gutierrez, I, Morris, DG, 2009. Influence of nanoprecipitates on the creep strength and ductility of a Fe–Ni–Al alloy. Int. J. Plast. 25, 1011–1023.
Nádai, Á, Wahl, AM, 1931. Plasticity, a mechanics of the plastic state of matter. J. Rheol. 2, 455–456.
Oberson, PG, Ankem, S, 2009. The effect of time-dependent twinning on low temperature (<0.25*Tm) creep of an alpha-titanium alloy. Int. J. Plast. 25, 881–900.
Reti, AM, Flemings, MC, 1972. Solution kinetics of two wrought aluminum alloys. Metall. Mater. Trans. B 3, 1869–1875.
Rioja, R, Liu, J, 2012. The evolution of Al-Li base products for aerospace and space applications. Metall. Mater. Trans. A 43, 3325–3337.
Rong, Q, Shi, Z, Li, Y, Lin, J, 2021. Constitutive modelling and its application to stress-relaxation age forming of AA6082 with elastic and plastic loadings. J. Mater. Process. Technol. 295, 117168.
Sallah, M, Peddieson, J, Foroudastan, S, 1991. A mathematical model of autoclave age forming. J Mater. Process. Technol. 28, 211–219.
Shercliff, HR, Ashby, MF, 1990. A process model for age hardening of aluminium alloys–1. The model. Acta Metall. Mater. 38, 1789–1802.
Shishvan, S, 2021. High-temperature tensile and creep behavior of Cu–Nb composites: a discrete dislocation plasticity investigation. Int. J. Plast. 136, 102876.
Svoboda, J, Fischer, FD, Riedel, H, Kozeschnik, E, 2016. Precipitate growth in multi-component systems with stress relaxation by diffusion and creep. Int. J. Plast. 82, 112–126.
Wang, S, Luo, J, Hou, L, Zhang, J, Zhuang, L, 2017. Identification of the threshold stress and true activation energy for characterizing the deformation mechanisms during hot working. Mater. Des. 113, 27–36.
Wang, X, Li, Y, Chen, B, Shi, Z, 2021. Development and trend of unified mechanism-based materials modelling for creep age forming of aluminium alloys. IOP Conf. Ser. Mater. Sci. Eng. 1024, 12021.
Wang, X, Rong, Q, Shi, Z, Li, Y, Cao, J, Chen, B, Lin, J, 2022. Investigation of stress effect on creep, precipitation and dislocation evolution of Al–Li alloy during creep age forming. Mater. Sci. Eng. A 836, 142723.
Xu, Y, Zhan, L, Li, W, 2017. Effect of pre-strain on creep aging behavior of 2524 aluminum alloy. J. Alloys Compd. 691, 564–571.
Yang, Y, Zhan, L, Liu, C, Wang, X, Wang, Q, Tang, Z, Li, G, Huang, M, Hu, Z, 2020. Stress-relaxation ageing behavior and microstructural evolution under varying initial stresses in an Al–Cu alloy: experiments and modeling. Int. J. Plast. 127, 102646.
Yang, Y, Zhan, L, Shen, R, Yin, X, Li, X, Li, W, Huang, M, He, D, 2017. Effect of pre-deformation on creep age forming of 2219 aluminum alloy: experimental and constitutive modelling. Mater. Sci. Eng. A 683, 227–235.
Yao, H, Xuan, F, Wang, Z, Tu, S, 2007. A review of creep analysis and design under multi-axial stress states. Nucl. Eng. Des. 237, 1969–1986.
Zhan, L, Lin, J, Dean, TA, Huang, M, 2011. Experimental studies and constitutive modelling of the hardening of aluminium alloy 7055 under creep age forming conditions. Int. J. Mech. Sci. 53, 595–605.
Zhang, J, Li, Z, Xu, F, Huang, C, 2019. Regulating effect of pre-stretching degree on the creep aging process of Al-Cu-Li alloy. Mater. Sci. Eng. A 763, 138157.
Zheng, J, Lin, J, Lee, J, Pan, R, Li, C, Davies, C, 2018. A novel constitutive model for multi-step stress relaxation ageing of a pre-strained 7xxx series alloy. Int. J. Plast. 106, 31–47.
Zhou, C, Zhan, L, Li, H, 2021. Improving creep age formability of an Al-Cu-Li alloy by electropulsing. J. Alloys Compd. 870, 159482.